WZ production at hadron colliders: Effects of nonstandard WWZ couplings and QCD corrections

U. Baur
Department of Physics, Florida State University, Tallahassee, Florida 32306
and Department of Physics, State University of New York at Buffalo, Buffalo, New York 14260

T. Han and J. Ohnemus
Department of Physics, University of California, Davis, California 95616
(Received 12 October 1994)

The process $p\overset{(-)}{p} \to W^{\pm}Z + X \to \ell_1^{\pm}\nu_1\ell_2^{+}\ell_2^{-} + X$ is calculated to $O(\alpha_s)$ for general C- and P-conserving WWZ couplings. At the Fermilab Tevatron center-of-mass energy, the QCD corrections to WZ production are modest. At CERN Large Hadron Collider (LHC) energies, the inclusive QCD corrections are large, but can be reduced significantly if a jet veto is imposed. The sensitivity limits for the anomalous WWZ couplings are derived from the next-to-leading-order Z boson transverse momentum distribution for Tevatron and LHC energies. Unless a jet veto is imposed, $O(\alpha_s)$ QCD corrections decrease the sensitivity to anomalous WWZ couplings considerably at LHC energies, but have little influence at the Tevatron. We also study, at next-to-leading-order, rapidity correlations between the W and Z decay products, and the ZZ/WZ and $WZ/W\gamma$ cross section ratios. These quantities are found to be useful tools in searching for the approximate zero present in the standard model WZ helicity amplitudes. The prospects for observing the approximate amplitude zero at the Tevatron and the LHC are critically assessed.

PACS number(s): 13.85.Qk, 12.38.Bx, 14.70.Fm, 14.70.Hp

I. INTRODUCTION

The electroweak standard model (SM) based on an $SU(2) \otimes U(1)$ gauge theory has been remarkably successful in describing contemporary high energy physics experiments. The three vector boson couplings predicted by this non-Abelian gauge theory, however, remain largely untested. The production of WZ pairs at hadron colliders provides an excellent opportunity to study the WWZ vertex [1–5]. In addition, the reaction $p\overset{(-)}{p} \to W^{\pm}Z$ is of interest due to the presence of an approximate zero in the amplitude of the parton level subprocess $q_1\bar{q}_2 \to W^{\pm}Z$ [5] in the SM, which is similar in nature to the well-known radiation zero in the reaction $p\overset{(-)}{p} \to W^{\pm}\gamma$ [6]. In the SM, the WWZ vertex is completely fixed by the $SU(2) \otimes U(1)$ gauge structure of the electroweak sector. A measurement of the WWZ vertex thus provides a stringent test of the SM.

WZ production at hadron colliders has recently received attention due to the observation of a clean $W^+Z \to e^+\nu_e e^+e^-$ candidate event by the Collider Detector at Fermilab (CDF) Collaboration [7]. Double leptonic WZ decays are relatively background free and therefore provide an excellent testing ground for anomalous WWZ couplings. With an integrated luminosity of the order of 1 fb^{-1}, which is envisioned for the main injector era [8], a sufficient number of events should be available to commence a detailed investigation of the WWZ vertex in the $W^{\pm}Z \to \ell_1^{\pm}\nu_1\ell_2^{+}\ell_2^{-}$ channel (ℓ_1, $\ell_2 = e$, μ). The prospects for a precise measurement of the WWZ couplings in this channel would further improve if integrated luminosities on the order of 10 fb^{-1} could be achieved (a luminosity-upgraded Tevatron will henceforth be denoted by TeV*) and/or the energy of the Tevatron could be doubled to $\sqrt{s} = 3.5$–4 TeV (an energy upgraded Tevatron will henceforth be referred to as the DiTevatron) [8]. At the CERN Large Hadron Collider [(LHC), pp collisions at $\sqrt{s} = 14$ TeV [9]], it should be possible to determine the WWZ couplings with high precision [3].

In contrast to low energy data and high precision measurements at the Z peak, collider experiments offer the possibility of a direct, and essentially model-independent, determination of the three vector boson vertices. Hadronic production of WZ pairs was first calculated in Ref. [1]. The $O(\alpha_s)$ QCD corrections to the reaction $p\overset{(-)}{p} \to W^{\pm}Z$ were first evaluated in Refs. [10] and [11]. Studies on the potential for probing the WWZ vertex have been performed in Refs. [3] and [4].

Previous studies on probing the WWZ vertex via hadronic WZ production have been based on leading-order (LO) calculations [3,4]. In general, the inclusion of anomalous couplings at the WWZ vertex yields enhancements in the WZ cross section, especially at large values of the W or Z boson transverse momentum $p_T(W)$ or $p_T(Z)$ and at large values of the WZ invariant mass M_{WZ}. Next-to-leading-order (NLO) calculations of hadronic WZ production have shown that the $O(\alpha_s)$ corrections are large in precisely these same regions [10,11]. It is thus vital to include the $O(\alpha_s)$ corrections when using hadronic WZ production to test the WWZ vertex for anomalous couplings.

In this paper, we calculate hadronic WZ production to $O(\alpha_s)$, including the most general, C- and P-conserving, anomalous WWZ couplings. Our calculation also in-

cludes the leptonic decays of the W and Z bosons in the narrow width approximation. Decay channels where the W or Z boson decays hadronically are not considered here. The calculation has been performed using the Monte Carlo method for NLO calculations [12]. With this method, it is easy to calculate a variety of observables simultaneously and to implement experimental acceptance cuts in the calculation. It is also possible to compute the $O(\alpha_s)$ QCD corrections for exclusive channels, e.g., $p\overset{(-)}{p} \to WZ + 0$ jet. Apart from anomalous contributions to the WWZ vertex we assume the SM to be valid in our calculation. In particular, we assume that the couplings of the W and Z bosons to quarks and leptons are as given by the SM. Section II briefly summarizes the technical details of our calculation.

The results of our numerical simulations are presented in Secs. III and IV. In contrast with the SM contributions to the $q_1\bar{q}_2 \to WZ$ helicity amplitudes, terms associated with nonstandard WWZ couplings grow with energy. The WZ invariant mass distribution, the cluster transverse mass distribution, and the Z boson transverse momentum spectrum are therefore very sensitive to anomalous WWZ couplings. In Sec. III, we focus on the impact QCD corrections have on these distributions, and the sensitivity limits for the anomalous WWZ couplings which can be achieved at the Tevatron, DiTevatron, and LHC with various integrated luminosities. At LHC energies, the inclusive $O(\alpha_s)$ QCD corrections in the SM are found to be very large at high $p_T(W)$ or $p_T(Z)$, and have a non-negligible influence on the sensitivity bounds which can be achieved for anomalous WWZ couplings. The large QCD corrections are caused by the combined effects of destructive interference in the Born subprocess, a log-squared enhancement factor in the $q_1 g \to WZq_2$ partonic cross section at high transverse momentum [11], and the large quark-gluon luminosity at supercollider energies. At the Tevatron, on the other hand, the $O(\alpha_s)$ QCD corrections are modest and sensitivities are only slightly affected by the QCD corrections. In Sec. III, we also show that the size of the QCD corrections at high $p_T(Z)$ or $p_T(W)$ can be significantly reduced, and a significant fraction of the sensitivity lost at LHC energies can be regained, if a jet veto is imposed, i.e., if the $WZ + 0$ jet exclusive channel is considered. We also find that the residual dependence of the NLO $WZ+0$ jet cross section on the factorization scale Q^2 is significantly smaller than that of the $O(\alpha_s)$ cross section for the inclusive reaction $p\overset{(-)}{p} \to WZ + X$.

In Sec. IV, we study rapidity correlations between the W and Z decay products, the ZZ/WZ and $WZ/W\gamma$ cross section ratios, and how these quantities are affected by QCD corrections. In the SM at the tree level, the process $q_1\bar{q}_2 \to WZ$ exhibits an approximate amplitude zero at $\cos\Theta^* \approx \frac{1}{3}\tan^2\theta_W \approx 0.1$ ($\cos\Theta^* \approx -\frac{1}{3}\tan^2\theta_W \approx -0.1$) for $u\bar{d} \to W^+Z$ ($d\bar{u} \to W^-Z$) [5] which is similar in nature to the well-known radiation zero in $W\gamma$ production in hadronic collisions. Here Θ^* is the Z boson scattering angle in the parton center-of-mass frame relative to the quark direction and θ_W is the weak mixing angle. The radiation zero in $W\gamma$ production can be observed rather easily at the Tevatron in the distribution of the rapidity difference $\Delta y(\gamma,\ell) = y(\gamma) - y(\ell)$ of the photon and the charged lepton which originates from the W decay, $W \to \ell\nu$ [13]. In the SM, the $\Delta y(\gamma,\ell)$ distribution exhibits a pronounced dip at $\Delta y(\gamma,\ell) \approx \mp 0.3$ in $W^\pm\gamma$ production, which originates from the radiation zero. We find that, at leading-order, the approximate amplitude zero in $p\overset{(-)}{p} \to W^\pm Z \to \ell_1^\pm\nu_1\ell_2^+\ell_2^-$ leads to a dip in the corresponding $\Delta y(Z,\ell_1) = y(Z) - y(\ell_1)$ distribution which is located at $\Delta y(Z,\ell_1) \approx \pm 0.5$ ($= 0$) in $p\bar{p}$ (pp) collisions. $O(\alpha_s)$ QCD corrections tend to fill in the dip; at LHC energies they obscure the signal of the approximate amplitude zero almost completely, unless a jet veto is imposed.

Alternatively, cross section ratios can be considered. Analogous to the $Z\gamma/W\gamma$ cross section ratio [14], the ZZ/WZ cross section ratio as a function of the minimum transverse momentum of the Z boson is found to reflect the approximate amplitude zero. The ratio of the WZ to $W\gamma$ cross sections, on the other hand, measures the relative strength of the radiation zero in $W\gamma$ production and the approximate zero in $q_1\bar{q}_2 \to WZ$. QCD corrections significantly affect the ratio of ZZ to WZ cross sections, but largely cancel in the $WZ/W\gamma$ cross section ratio. Although rapidity correlations and cross section ratios are useful tools in searching for the approximate amplitude zero in WZ production, it will not be easy to establish the effect at the Tevatron or LHC, due to the limited number of $W^\pm Z \to \ell_1^\pm\nu_1\ell_2^+\ell_2^-$ events expected. Our conclusions, finally, are given in Sec. V.

II. CALCULATIONAL TOOLS

Our calculation generalizes the results of Ref. [15] to arbitrary C- and P-conserving WWZ couplings. It is carried out using a combination of analytic and Monte Carlo integration techniques. Details of the method can be found in Ref. [12]. The calculation is done using the narrow width approximation for the leptonically decaying W and Z bosons. In this approximation it is particularly easy to extend the NLO calculation of WZ production with on-shell W and Z bosons to include the leptonic W and Z decays. Furthermore, nonresonant Feynman diagrams such as $d\bar{u} \to W^{-*} \to e^-\bar{\nu}_e Z$ followed by $Z \to \mu^+\mu^-$ contribute negligibly in this limit, and thus can be ignored.

A. Summary of $O(\alpha_s)$ WZ production including W and Z decays

The NLO calculation of WZ production includes contributions from the square of the Born graphs, the interference between the Born graphs and the virtual one-loop diagrams, and the square of the real emission graphs. The basic idea of the method employed here is to isolate the soft and collinear singularities associated with the real emission subprocesses by partitioning phase space into soft, collinear, and finite regions. This is done by in-

troducing theoretical soft and collinear cutoff parameters δ_s and δ_c. Using dimensional regularization, the soft and collinear singularities are exposed as poles in ϵ (the number of space-time dimensions is $N = 4 - 2\epsilon$ with ϵ a small number). The infrared singularities from the soft and virtual contributions are then explicitly canceled while the collinear singularities are factorized and absorbed into the definition of the parton distribution functions. The remaining contributions are finite and can be evaluated in four dimensions. The Monte Carlo program thus generates n-body (for the Born and virtual contributions) and $(n+1)$-body (for the real emission contributions) final state events. The n- and $(n+1)$-body contributions both depend on the cutoff parameters δ_s and δ_c; however, when these contributions are added together to form a suitably inclusive observable, all dependence on the cutoff parameters cancels. The numerical results presented in this paper are insensitive to variations of the cutoff parameters.

Except for the virtual contribution, the $O(\alpha_s)$ corrections are all proportional to the Born cross section. It is easy to incorporate the decays $W \to \ell_1 \nu_1$ and $Z \to \ell_2^+ \ell_2^-$ into those terms which are proportional to the Born cross section; one simply replaces $d\hat{\sigma}^{\rm Born}(q_1\bar{q}_2 \to WZ)$ with $d\hat{\sigma}^{\rm Born}(q_1\bar{q}_2 \to WZ \to \ell_1\nu_1\ell_2^+\ell_2^-)$ in the relevant formulas. When working at the amplitude level, the W and Z decays are trivial to implement; the vector boson polarization vector $\epsilon_\mu^V(k)$, $V = W, Z$, is simply replaced by the respective decay current $J_\mu^V(k)$ in the amplitude. Details of the amplitude level calculations for the Born and real emission subprocesses can be found in Ref. [16]. For $\ell_1 = \ell_2$ the amplitudes in principle should be antisymmetrized. Since the leptons originating from the decay of the W and Z bosons are usually well separated, effects from the antisymmetrization of the amplitudes are expected to be very small and hence are ignored here.

The only term in which it is more difficult to incorporate the W and Z decays is the virtual contribution. Rather than undertake the nontrivial task of recalculating the virtual correction term for the case of leptonically decaying weak bosons, we have instead opted to use the virtual correction for real on-shell W and Z bosons which we subsequently decay ignoring spin correlations. When spin correlations are ignored, the spin-summed-squared matrix element factorizes into separate production and decay-squared matrix elements.

Neglecting spin correlations slightly modifies the shapes of the angular distributions of the final state leptons, but does not alter the total cross section as long as no angular cuts (e.g., rapidity cuts) are imposed on the final state leptons. For realistic rapidity cuts, cross sections are changed by typically 10% if spin correlations are neglected. Since the size of the finite virtual correction is less than $\sim 10\%$ the size of the Born cross section, the overall effect of neglecting the spin correlations in the finite virtual correction is expected to be negligible compared to the combined 10%–20% uncertainty from the parton distribution functions, the choice of the scale Q^2, and higher-order QCD corrections.

B. Incorporation of anomalous WWZ couplings

The WWZ vertex is uniquely determined in the SM by $\mathrm{SU(2)} \bigotimes \mathrm{U(1)}$ gauge invariance. In WZ production the W and Z bosons couple to essentially massless fermions, which ensures that effectively $\partial_\mu W^\mu = 0$ and $\partial_\mu Z^\mu = 0$. These conditions together with Lorentz invariance and conservation of C and P allow three free parameters g_1, κ, and λ, in the WWZ vertex. The most general Lorentz-, C-, and P-invariant vertex is described by the effective Lagrangian [17]

$$\mathcal{L}_{WWZ} = -ie\cot\theta_{\rm W}\left[g_1\left(W^\dagger_{\mu\nu}W^\mu Z^\nu - W^\dagger_\mu Z_\nu W^{\mu\nu}\right) + \kappa W^\dagger_\mu W_\nu Z^{\mu\nu} + \frac{\lambda}{M_W^2}W^\dagger_{\lambda\mu}W^\mu_\nu Z^{\nu\lambda}\right], \tag{1}$$

where W^μ and Z^μ are the W^- and Z fields, respectively, $W_{\mu\nu} = \partial_\mu W_\nu - \partial_\nu W_\mu$, and $Z_{\mu\nu} = \partial_\mu Z_\nu - \partial_\nu Z_\mu$. At the tree level in the SM, $g_1 = 1$, $\kappa = 1$, and $\lambda = 0$. All higher dimensional operators are obtained by replacing V^μ with $(\partial^2)^m V^\mu$, $V = W, Z$, where m is an arbitrary positive integer, in the terms proportional to $\Delta g_1 = g_1 - 1$, $\Delta\kappa = \kappa - 1$, and λ. These operators form a complete set and can be summed by replacing Δg_1, $\Delta\kappa$, and λ by momentum-dependent form factors. All details are contained in the specific functional form of the form factor and its scale $\Lambda_{\rm FF}$. The form factor nature of Δg_1, $\Delta\kappa$, and λ will be discussed in more detail later in this section.

Following the standard notation of Ref. [17], we have chosen, without loss of generality, the W boson mass, M_W, as the energy scale in the denominator of the term proportional to λ in Eq. (1). If a different mass scale $\mathtt{M}$ had been used, then all of our subsequent results could be obtained by scaling λ by a factor $\mathtt{M}^2/M_W^2$.

At present, the WWZ coupling constants are only weakly constrained experimentally. The CDF Collaboration recently presented preliminary 95% confidence level (C.L.) limits on $\Delta\kappa$ and λ from a search performed in the $p\bar{p} \to WZ \to jj\ell^+\ell^-$ ($\ell = e, \mu$) channel at large dijet transverse momenta $p_T(jj) > 100$ GeV [7]:

$$-8.6 < \Delta\kappa < 9.0 \quad (\text{for } \lambda = 0)\,,$$
$$-1.7 < \lambda < 1.7 \quad (\text{for } \Delta\kappa = 0)\,. \tag{2}$$

Assuming SM $WW\gamma$ couplings, CDF also obtained a limit on $\Delta\kappa$ from the reactions $p\bar{p} \to W^+W^-$, $W^\pm Z \to \ell^\pm\nu jj$ with $p_T(jj) > 130$ GeV [7,18]:

$$-1.3 < \Delta\kappa < 1.4 \quad (\text{for } \lambda = 0)\,. \tag{3}$$

To derive these limits, a dipole form factor with scale $\Lambda_{\rm FF} = 1.5$ TeV was assumed (see below); however, the experimental bounds are quite insensitive to the value of $\Lambda_{\rm FF}$. Although bounds on these couplings can also be extracted from low energy data and high precision measurements at the Z pole, there are ambiguities and model dependences in the results [19–21]. From loop contributions to rare meson decays such as $K_L \to \mu^+\mu^-$ [22] or $B \to K^{(*)}\mu^+\mu^-$ [23], ϵ'/ϵ [24], and the $Z \to b\bar{b}$ width [25], one estimates limits for the nonstandard WWZ couplings of $\sim 1 - 10$. No rigorous bounds can be obtained from LEP I data if correlations between different contributions to the anomalous couplings are taken fully into account. In contrast, invoking a "naturalness" argument based on chiral perturbation theory [26,27], one expects deviations from the SM of $\sim 10^{-2}$ or less for g_1, κ, and λ.

If C- or P-violating WWZ couplings are allowed, four additional free parameters g_4, g_5, $\tilde{\kappa}$, and $\tilde{\lambda}$ appear in the effective Lagrangian. For simplicity, these couplings are not considered in this paper.

The Feynman rule for the WWZ vertex factor corresponding to the Lagrangian in Eq. (1) is

$$-i\,g_{WWZ}\,Q_W\,\Gamma_{\beta\mu\nu}(k,k_1,k_2) = -i\,g_{WWZ}\,Q_W\left[\Gamma^{\rm SM}_{\beta\mu\nu}(k,k_1,k_2) + \Gamma^{\rm NSM}_{\beta\mu\nu}(k,k_1,k_2)\right], \tag{4}$$

where the labeling conventions for the four-momenta and Lorentz indices are defined by Fig. 1, $g_{WWZ} = e\cot\theta_{\rm W}$ is the WWZ coupling strength, Q_W is the electric charge of the W boson in units of the proton charge e, and the factors $\Gamma^{\rm SM}$ and $\Gamma^{\rm NSM}$ are the SM and nonstandard model (NSM) vertex factors:

$$\Gamma^{\rm SM}_{\beta\mu\nu}(k,k_1,k_2) = (k_1-k_2)_\beta\,g_{\nu\mu} + 2\,k_\mu\,g_{\beta\nu} - 2\,k_\nu\,g_{\beta\mu}\,, \tag{5}$$

$$\Gamma^{\rm NSM}_{\beta\mu\nu}(k,k_1,k_2) = \frac{1}{2}\left(\Delta g_1 + \Delta\kappa + \lambda\frac{k^2}{M_W^2}\right)(k_1-k_2)_\beta\,g_{\nu\mu} - \frac{\lambda}{M_W^2}(k_1-k_2)_\beta\,k_\nu\,k_\mu + (\Delta g_1 + \Delta\kappa + \lambda)\,k_\mu\,g_{\beta\nu} - \left(2\Delta g_1 + \lambda\frac{M_Z^2}{M_W^2}\right)k_\nu\,g_{\beta\mu}\,. \tag{6}$$

The nonstandard model vertex factor is written here in terms of $\Delta g_1 = g_1 - 1$, $\Delta\kappa = \kappa - 1$, and λ, which all vanish in the SM.

It is straightforward to include the nonstandard model couplings in the amplitude level calculations. Using the computer algebra program FORM [28], we have computed the $q_1\bar{q}_2 \to WZ$ virtual correction with the modified vertex factor of Eq. (4); however, the resulting expression is too lengthy to present here. The nonstandard WWZ couplings of Eq. (1) do not destroy the renormalizability of QCD. Thus the infrared singularities from the soft and virtual contributions are explicitly canceled, and the collinear singularities are factorized and absorbed into the definition of the parton distribution functions, exactly as in the SM case.

The anomalous couplings cannot be simply inserted into the vertex factor as constants because this would violate S-matrix unitarity. Tree level unitarity uniquely restricts the WWZ couplings to their SM gauge theory values at asymptotically high energies [29]. This implies that any deviation of Δg_1, $\Delta\kappa$, or λ from the SM expectation has to be described by a form factor $\Delta g_1(M^2_{WZ}, p^2_W, p^2_Z)$, $\Delta\kappa(M^2_{WZ}, p^2_W, p^2_Z)$, or $\lambda(M^2_{WZ}, p^2_W, p^2_Z)$ which vanishes when either the square of the WZ invariant mass M^2_{WZ} or the square of the four-momentum of the final state W or Z (p^2_W or p^2_Z) becomes large. In WZ production $p^2_W \approx M^2_W$ and $p^2_Z \approx M^2_Z$ even when the finite W and Z widths are taken into account. However, large values of M^2_{WZ} will be probed at future hadron colliders like the LHC and the M^2_{WZ} dependence of the anomalous couplings has to be included in order to avoid unphysical results which would violate unitarity. Consequently, the anomalous couplings are introduced via form factors [30,31]

$$\Delta g_1(M^2_{WZ}, p^2_W = M^2_W, p^2_Z = M^2_Z) = \frac{\Delta g_1^0}{(1 + M^2_{WZ}/\Lambda^2_{\rm FF})^n}\,, \tag{7}$$

$$\Delta\kappa(M^2_{WZ}, p^2_W = M^2_W, p^2_Z = M^2_Z) = \frac{\Delta\kappa^0}{(1 + M^2_{WZ}/\Lambda^2_{\rm FF})^n}\,, \tag{8}$$

$$\lambda(M^2_{WZ}, p^2_W = M^2_W, p^2_Z = M^2_Z) = \frac{\lambda^0}{(1 + M^2_{WZ}/\Lambda^2_{\rm FF})^n}\,, \tag{9}$$

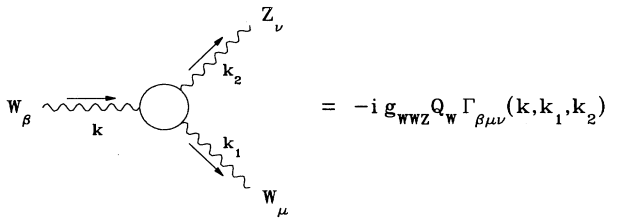

FIG. 1. Feynman rule for the general WWZ vertex. The factor $g_{WWZ} = e\cot\theta_W$ is the WWZ coupling strength and Q_W is the electric charge of the W boson. The vertex function $\Gamma_{\beta\mu\nu}(k,k_1,k_2)$ is given in Eq. (4).

where Δg_1^0, $\Delta\kappa^0$, and λ^0 are the form factor values at low energies and Λ_{FF} represents the scale at which new physics becomes important in the weak boson sector, e.g., due to new resonances or composite structures of the W and Z bosons. In order to guarantee unitarity, it is necessary to have $n > 1/2$ for $\Delta\kappa$ and $n > 1$ for Δg_1 and λ. For the numerical results presented here, we use a dipole form factor ($n = 2$) with a scale $\Lambda_{FF} = 1$ TeV, unless explicitly stated otherwise. The exponent $n = 2$ is chosen in order to suppress WZ production at energies $\sqrt{\hat{s}} > \Lambda_{FF} \gg M_W, M_Z$, where novel phenomena like resonance or multiple weak boson production are expected to become important.

Form factors are usually not introduced if an ansatz based on chiral perturbation theory is used. In the framework of chiral perturbation theory, the effective Lagrangian describing the anomalous vector boson self-interactions breaks down at center-of-mass energies above a few TeV [26,27] (typically $4\pi v \sim 3$ TeV, where $v \approx 246$ GeV is the Higgs field vacuum expectation value). Consequently, one has to limit the center-of-mass energies to values sufficiently below $4\pi v$ in this approach.

III. QCD CORRECTIONS AND NONSTANDARD WWZ COUPLINGS

We shall now discuss the phenomenological implications of $O(\alpha_s)$ QCD corrections to WZ production at the Tevatron ($p\bar{p}$ collisions at $\sqrt{s} = 1.8$ TeV) and the LHC (pp collisions at $\sqrt{s} = 14$ TeV). We also consider a possible upgrade [8] of the Tevatron to $\sqrt{s} = 3.5$ TeV (DiTevatron). We first briefly describe the input parameters, cuts, and the finite energy resolution smearing used to simulate detector response. We then discuss in detail the impact of $O(\alpha_s)$ QCD corrections on the observability of nonstandard WWZ couplings in WZ production at the Tevatron, DiTevatron, and LHC. To simplify the discussion, we shall concentrate on W^+Z production. In $p\bar{p}$ collisions the rates for W^+Z and W^-Z production are equal. At pp colliders, the W^-Z cross section is about 30% smaller than that of W^+Z production. Furthermore, we shall only consider $W^+ \to \ell_1^+\nu_1$ and $Z \to \ell_2^+\ell_2^-$ decays (ℓ_1, $\ell_2 = e$, μ).

A. Input parameters

The numerical results presented here were obtained using the two-loop expression for α_s. The QCD scale Λ_{QCD} is specified for four flavors of quarks by the choice of the parton distribution functions and is adjusted whenever a heavy quark threshold is crossed so that α_s is a continuous function of Q^2. The heavy quark masses were taken to be $m_b = 5$ GeV and $m_t = 150$ GeV, which is consistent with the bound obtained by D0, $m_t > 131$ GeV [32], and the value suggested by the current CDF data, $m_t = 174 \pm 10^{+13}_{-12}$ GeV [33]. Our results are insensitive to the value chosen for m_t.

The SM parameters used in the numerical simulations are $M_Z = 91.173$ GeV, $M_W = 80.22$ GeV, $\alpha(M_W) = 1/128$, and $\sin^2\theta_W = 1 - (M_W/M_Z)^2$. These values are consistent with recent measurements at the CERN e^+e^- collider LEP, SLAC Linear Collider (SLC), the CERN $p\bar{p}$ collider, and the Tevatron [34–37]. The soft and collinear cutoff parameters, as discussed in Sec. II A, are fixed to $\delta_s = 10^{-2}$ and $\delta_c = 10^{-3}$. The parton subprocesses have been summed over u, d, s, and c quarks and the Cabibbo mixing angle has been chosen such that $\cos^2\theta_C = 0.95$. The leptonic branching ratios have been taken to be $B(W \to \ell\nu) = 0.107$ and $B(Z \to \ell^+\ell^-) = 0.034$ and the total widths of the W and Z bosons are $\Gamma_W = 2.12$ GeV and $\Gamma_Z = 2.487$ GeV. Except where otherwise stated, a single scale $Q^2 = M_{WZ}^2$, where M_{WZ} is the invariant mass of the WZ pair, has been used for the renormalization scale μ^2 and the factorization scale M^2.

In order to get consistent NLO results it is necessary to use parton distribution functions which have been fit to next-to-leading-order. In our numerical simulations we have used the Martin-Roberts-Stirling (MRS) [38] set S0′ distributions with $\Lambda_4 = 230$ MeV, which take into account the most recent New Muon Collaboration (NMC) [39] and Chicago-Columbia-Fermilab-Rochester (CCFR) [40] data and are consistent with measurements of the proton structure functions at the DESY ep collider HERA [41]. For convenience, the MRS set S0′ distributions have also been used for the LO calculations.

B. Cuts

The cuts imposed in our numerical simulations are motivated by the finite acceptance of detectors. The complete set of transverse momentum (p_T), pseudorapidity (η), and separation cuts can be summarized as follows:

Tevatron	LHC
$p_T(\ell) > 20$ GeV	$p_T(\ell) > 25$ GeV
$\not{p}_T > 20$ GeV	$\not{p}_T > 50$ GeV
$\lvert\eta(\ell)\rvert < 2.5$	$\lvert\eta(\ell)\rvert < 3.0$
$\Delta R(\ell,\ell) > 0.4$	$\Delta R(\ell,\ell) > 0.4$

Here, $\Delta R = [(\Delta\phi)^2 + (\Delta\eta)^2]^{1/2}$ is the separation in the pseudorapidity–azimuthal-angle plane. The $\Delta R(\ell,\ell)$ cut is only imposed on leptons of equal electric charge. It has only a small effect on the WZ cross section. For simplicity, identical cuts are imposed on final state elec-

trons and muons. The large missing transverse momentum ($\not{p}_T$) cut at LHC energies, which severely reduces the total WZ cross section, has been chosen to reduce potentially dangerous backgrounds from event pileup [42], $pp \to Zb\bar{b} \to \ell_1\nu_1\ell_2^+\ell_2^- + X$, and processes where particles outside the rapidity range covered by the detector contribute to the missing transverse momentum. Present studies [43,44] indicate that these backgrounds are under control for $\not{p}_T > 50$ GeV. The total W^+Z cross section within cuts in the Born approximation at the Tevatron, DiTevatron, and LHC is 8.5 fb, 22.4 fb, and 25.9 fb, respectively. If the LHC is operated significantly below the design luminosity of $\mathcal{L} = 10^{34}\ \mathrm{cm}^{-2}\mathrm{s}^{-1}$ [9], the background from event pileup is less severe and it may well be possible to lower the missing p_T threshold. If the $\not{p}_T > 50$ GeV cut is replaced by a $\not{p}_T > 20$ GeV requirement, the total LO W^+Z cross section triples to 80.8 fb.

C. Finite energy resolution effects

Uncertainties in the energy measurements of the charged leptons in the detector are simulated in our calculation by Gaussian smearing of the particle four-momentum vector with standard deviation σ. For distributions which require a jet definition, e.g., the $WZ+1$ jet exclusive cross section, the jet four-momentum vector is also smeared. The standard deviation σ depends on the particle type and the detector. The numerical results presented here for the Tevatron and/or DiTevatron and LHC center-of-mass energies were made using σ values based on the CDF [45] and ATLAS [43] specifications, respectively.

D. Inclusive NLO cross sections

The sensitivity of WZ production to anomalous WWZ couplings in the Born approximation was studied in detail in Refs. [3] and [4]. The distributions of the Z boson transverse momentum, $p_T(Z)$, and the WZ invariant mass M_{WZ} were found to be sensitive to the anomalous couplings. However, at hadron colliders the WZ invariant mass cannot be determined unambiguously because the neutrino from the W decay is not observed. If the transverse momentum of the neutrino is identified with the missing transverse momentum of a given WZ event, the unobserved longitudinal neutrino momentum $p_L(\nu)$ can be reconstructed, albeit with a twofold ambiguity, by imposing the constraint that the neutrino and the charged lepton four-momenta combine to form the W rest mass [46,47]. Neglecting the lepton mass one finds

$$p_L(\nu) = \frac{1}{2\,p_T^2(\ell)}\left(p_L(\ell)\left[M_W^2 + 2\,\mathbf{p}_T(\ell)\cdot\not{\mathbf{p}}_T\right] \pm p(\ell)\left\{\left[M_W^2 + 2\,\mathbf{p}_T(\ell)\cdot\not{\mathbf{p}}_T\right]^2 - 4\,p_T^2(\ell)\,\not{p}_T^2\right\}^{1/2}\right), \tag{10}$$

where $p_L(\ell)$ denotes the longitudinal momentum of the charged lepton. The two solutions for $p_L(\nu)$ are used to reconstruct two values for M_{WZ}. Both values are then histogrammed, each with half the event weight.

The differential cross section for M_{WZ} in the reaction $p\bar{p} \to W^+Z + X \to \ell_1\nu_1\ell_2^+\ell_2^- + X$ at $\sqrt{s} = 1.8$ TeV is shown in Fig. 2. The Born and NLO results are shown in Fig. 2(a) and Fig. 2(b), respectively. In both cases, results are displayed for the SM and for three sets of anomalous couplings, namely ($\lambda^0 = -0.5$, $\Delta\kappa^0 = \Delta g_1^0 = 0$), ($\Delta\kappa^0 = -1.0$, $\lambda^0 = \Delta g_1^0 = 0$), and ($\Delta g_1^0 = -0.5$, $\Delta\kappa^0 = \lambda^0 = 0$). For simplicity, only one anomalous coupling

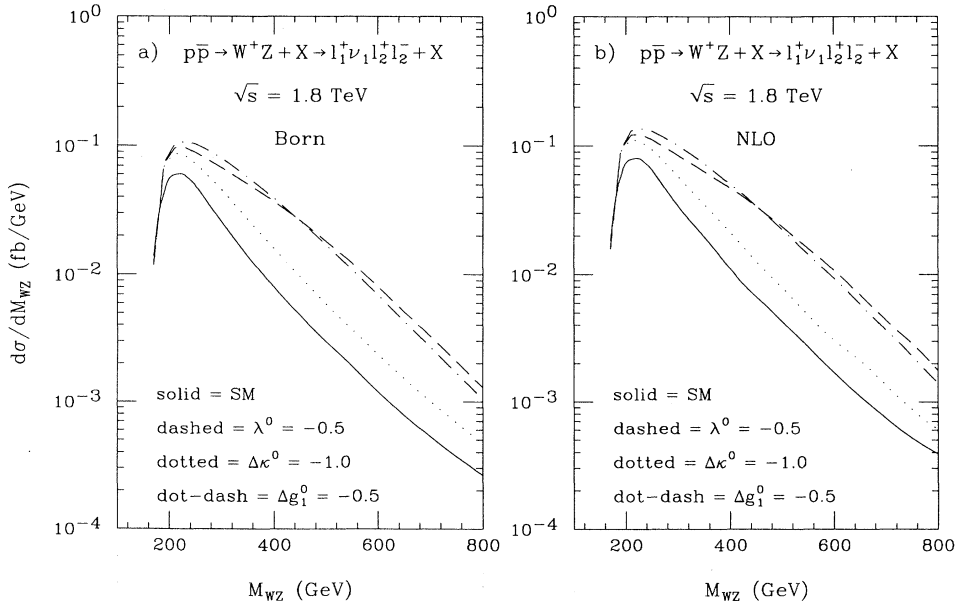

FIG. 2. The inclusive differential cross section for the reconstructed WZ mass in the reaction $p\bar{p} \to W^+Z + X \to \ell_1^+\nu_1\ell_2^+\ell_2^- + X$ at $\sqrt{s} = 1.8$ TeV (a) in the Born approximation and (b) including $O(\alpha_s)$ QCD corrections. The curves are for the SM (solid lines), $\lambda^0 = -0.5$ (dashed lines), $\Delta\kappa^0 = -1.0$ (dotted lines), and $\Delta g_1^0 = -0.5$ (dot-dashed lines). The cuts imposed are summarized in Sec. III B.

at a time is allowed to differ from its SM value. The figure shows that at the Tevatron center-of-mass energy, $O(\alpha_s)$ QCD corrections do not have a large influence on the sensitivity of the reconstructed WZ invariant mass distribution to anomalous couplings. The $O(\alpha_s)$ corrections at Tevatron energies are approximately 30% for the SM as well as for the anomalous coupling cases. Since the anomalous terms in the helicity amplitudes grow like $\sqrt{\hat{s}}/M_W$ ($\hat{s}/M_W^2$) for $\Delta\kappa$ (λ and Δg_1) [3], where $\hat{s}$ denotes the parton center-of-mass energy squared, nonstandard couplings give large enhancements in the cross section at large values of M_{WZ}.

The WZ invariant mass distributions at the DiTevatron and the LHC are shown in Figs. 3 and 4, respectively. In both cases, the sensitivity of the M_{WZ} distribution to anomalous WWZ couplings is significantly more pronounced than for $p\bar{p}$ collisions at $\sqrt{s} = 1.8$ TeV. $O(\alpha_s)$ QCD corrections enhance the SM M_{WZ} differential cross section by about a factor 2 at the LHC, whereas the $O(\alpha_s)$ corrections at the DiTevatron are very similar in size to those found at Tevatron energies. For nonstandard WWZ couplings, the QCD corrections are more modest at the LHC. Because of the form factor parameters assumed, the result for $\Delta\kappa^0 = -1$ approaches the SM result at large values of M_{WZ}. As mentioned before, we have used $n = 2$ and a form factor scale of $\Lambda_{\rm FF} = 1$ TeV in all our numerical simulations [see Eqs. (7)–(9)]. For a larger scale $\Lambda_{\rm FF}$, the deviations from the SM result become more pronounced at high energies. No significant change in the shape of the M_{WZ} distribution is observed for all center-of-mass energies considered.

In Fig. 5 we investigate the influence of anomalous WWZ couplings on the WZ invariant mass spectrum at next-to-leading-order, together with the effect of the twofold ambiguity in M_{WZ} originating from the reconstruction of the longitudinal momentum of the neutrino from the W decay, in more detail. The lower dotted, dashed, and dot-dashed lines display the WZ invariant mass distribution for $\Delta\kappa^0 = +1$ (+1), $\Delta g_1^0 = +0.5$ (+0.25), and $\lambda^0 = +0.5$ (+0.25), whereas the upper curves show the M_{WZ} spectrum for $\Delta\kappa^0 = -1$ (−1), $\Delta g_1^0 = -0.5$ (−0.25), and $\lambda^0 = -0.5$ (−0.25) at the Tevatron (LHC). For $\Delta\kappa^0$ and Δg_1^0, negative anomalous couplings lead to significantly larger deviations from the SM prediction than positive nonstandard couplings of equal magnitude, whereas there is little difference for λ^0 (dashed lines). For $\Delta\kappa^0$ the sign dependence is more pronounced at small energies. Other distributions, such as the cluster transverse mass distribution or the transverse momentum distribution of the Z boson, display a similar behavior.

This effect can be easily understood from the high energy behavior of the WZ production amplitudes, $\mathcal{M}(\lambda_Z, \lambda_W)$, where λ_Z (λ_W) denotes the helicity of the Z (W) boson [3,5]. In the SM, only $\mathcal{M}(\pm, \mp)$ and $\mathcal{M}(0,0)$ remain finite for $\hat{s} \to \infty$. Contributions to the helicity amplitudes proportional to λ mostly influence the $(\pm,\pm)$ amplitudes and increase like $\hat{s}/M_W^2$ at large energies. The SM $(\pm,\pm)$ amplitudes vanish like $1/\hat{s}$, and nonstandard terms dominate except for the threshold region, $\sqrt{\hat{s}} \approx M_W + M_Z$. For nonstandard values of λ, the cross section therefore depends only very little on the sign of the anomalous coupling. Terms proportional to Δg_1 also increase like $\hat{s}/M_W^2$ with energy, but mostly contribute to the (0,0) amplitude, which remains finite in the SM in the high energy limit. Interference effects between the SM and the anomalous contributions to the (0,0) amplitude, thus, are non-negligible, resulting in a significant dependence of the cross section on the sign of Δg_1. Terms proportional to $\Delta\kappa$, finally, are proportional to $\sqrt{\hat{s}}/M_W$ and mostly influence the amplitudes with a longitudinal W and a transverse Z boson. In the

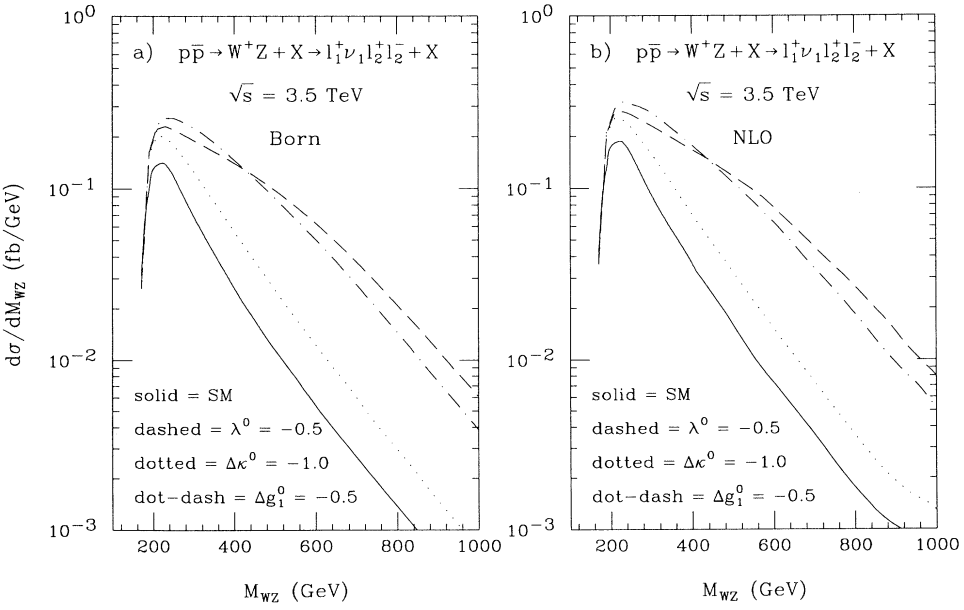

FIG. 3. The inclusive differential cross section for the reconstructed WZ mass in the reaction $p\bar{p} \to W^+Z + X \to \ell_1^+\nu_1\ell_2^+\ell_2^- + X$ at $\sqrt{s}$ = 3.5 TeV (a) in the Born approximation and (b) including $O(\alpha_s)$ QCD corrections. The curves are for the SM (solid lines), $\lambda^0 = -0.5$ (dashed lines), $\Delta\kappa^0 = -1.0$ (dotted lines), and $\Delta g_1^0 = -0.5$ (dot-dashed lines). The cuts imposed are summarized in Sec. III B.

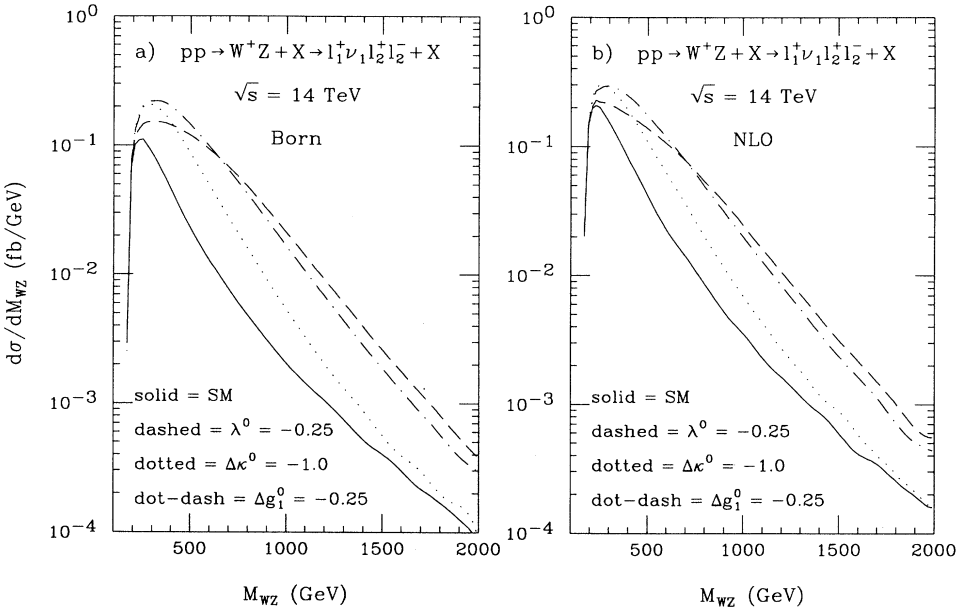

FIG. 4. The inclusive differential cross section for the reconstructed WZ mass in the reaction $pp \to W^+Z + X \to \ell_1^+\nu_1\ell_2^+\ell_2^- + X$ at $\sqrt{s}$ = 14 TeV (a) in the Born approximation and (b) including $O(\alpha_s)$ QCD corrections. The curves are for the SM (solid lines), $\lambda^0 = -0.25$ (dashed lines), $\Delta\kappa^0 = -1.0$ (dotted lines), and $\Delta g_1^0 = -0.25$ (dot-dashed lines). The cuts imposed are summarized in Sec. III B.

SM, these terms vanish like $1/\sqrt{\hat{s}}$. In the high energy limit one therefore expects little dependence of the cross section on the sign of $\Delta\kappa$, similar to the situation encountered for λ [see Fig. 5(b)]. However, since the terms proportional to $\Delta\kappa$ increase less drastically with energy, interference effects between those terms and the SM amplitudes are substantial near threshold.

The double-dotted-dashed line in Fig. 5 shows the true M_{WZ} distribution. The distribution of the reconstructed invariant mass at both center-of-mass energies is harder than the true M_{WZ} distribution. At LHC energies, the twofold ambiguity in the reconstructed WZ invariant mass only slightly affects the M_{WZ} distribution [Fig. 5(b)]. At the Tevatron, on the other hand, the true and reconstructed invariant masses are quite different for $M_{WZ} > 500$ GeV, thus severely degrading the sensitivity to nonstandard WWZ couplings. If the W decay is treated in the narrow width approximation, one of the two reconstructed invariant masses coincides with the true WZ invariant mass. Since the M_{WZ} spectrum is steeply falling, the incorrect solution of the reconstructed invariant mass influences the distribution in a noticeable way only if it is larger than the true WZ invariant mass. The average difference (absolute value) between the two reconstructed values of M_{WZ} is almost independent of the center-of-mass energy. As a result, the twofold am-

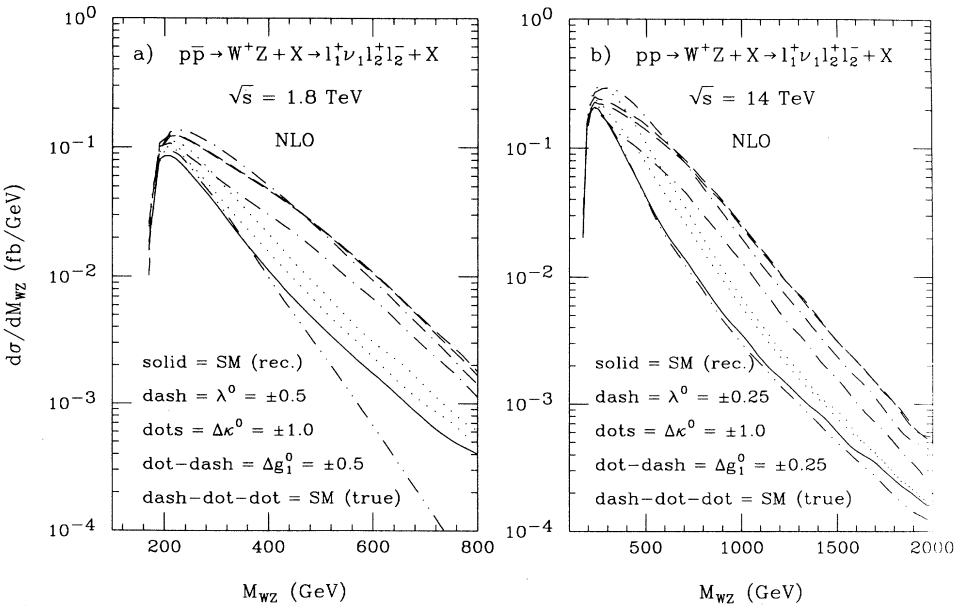

FIG. 5. The inclusive NLO differential cross section for the reconstructed WZ mass in the reaction (a) $p\bar{p} \to W^+Z + X \to \ell_1^+\nu_1\ell_2^+\ell_2^- + X$ at $\sqrt{s}$ = 1.8 TeV and (b) $pp \to W^+Z + X \to \ell_1^+\nu_1\ell_2^+\ell_2^- + X$ at $\sqrt{s}$ = 14 TeV. The curves are for the SM with reconstructed invariant mass (solid lines) and nonstandard WWZ couplings (dotted, dashed, and dot-dashed curves) as listed in the figure. The lower (upper) lines apply for positive (negative) anomalous couplings. The double-dotted-dashed line shows the true SM WZ invariant mass distribution. The cuts imposed are summarized in Sec. III B.

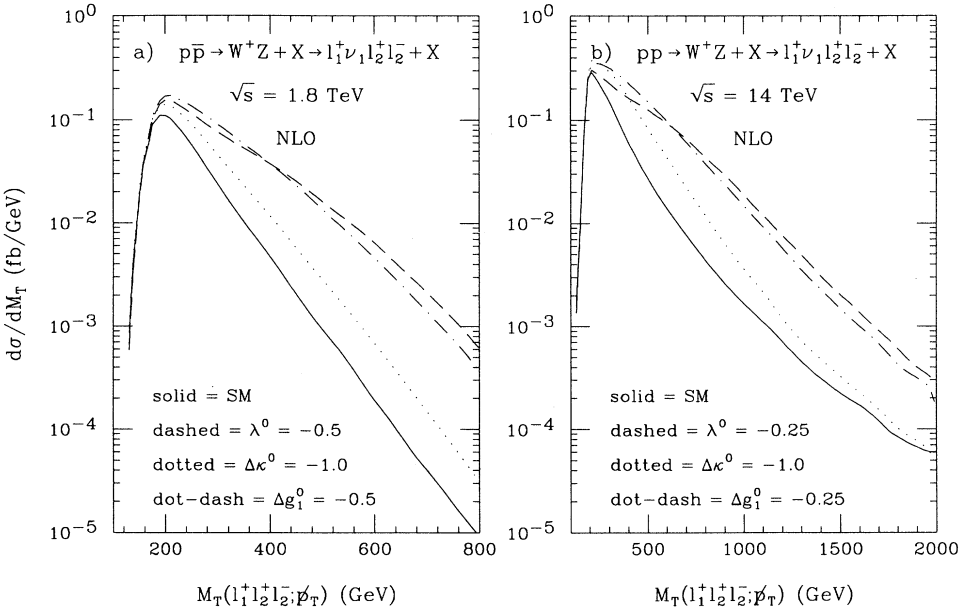

FIG. 6. The inclusive NLO differential cross section for the cluster transverse mass for (a) $p\bar{p} \to W^+Z + X \to \ell_1^+\nu_1\ell_2^+\ell_2^- + X$ at $\sqrt{s} = 1.8$ TeV and (b) $pp \to W^+Z + X \to \ell_1^+\nu_1\ell_2^+\ell_2^- + X$ at $\sqrt{s} = 14$ TeV. The curves are for the SM (solid lines) and nonstandard WWZ couplings (dotted, dashed, and dot-dashed curves) as listed on the figure. The cuts imposed are summarized in Sec. III B.

biguity in the reconstructed WZ invariant mass affects the M_{WZ} spectrum at the LHC much less than at the Tevatron.

As an alternative to the WZ invariant mass spectrum, the differential cross section of the cluster transverse mass $M_T(\ell_1\ell_2^+\ell_2^-;\not{p}_T)$ [48] can be studied. The cluster transverse mass is defined by

$$M_T^2(c;\not{p}_T) = \left\{\left[M_c^2 + |\mathbf{p}_T(c)|^2\right]^{1/2} + \not{p}_T\right\}^2 - |\mathbf{p}_T(c) + \not{\mathbf{p}}_T|^2, \quad (11)$$

where M_c denotes the invariant mass of the cluster $c = \ell_1\ell_2^+\ell_2^-$. The M_T distribution at the Tevatron and the LHC is shown in Fig. 6. Since QCD corrections change its shape only slightly, we only show the NLO M_T distribution. At the Tevatron, the cluster transverse mass distribution is seen to be significantly more sensitive to anomalous couplings than the reconstructed WZ invariant mass distribution, in particular for λ and Δg_1. The cluster transverse mass distribution for $p\bar{p}$ collisions at $\sqrt{s} = 3.5$ TeV is qualitatively very similar to that obtained at Tevatron energies and is therefore not shown.

In Figs. 7–9 we show the differential cross section for the transverse momentum of the Z boson, $p_T(Z)$. The $p_T(Z)$ spectrum is seen to be considerably more sensi-

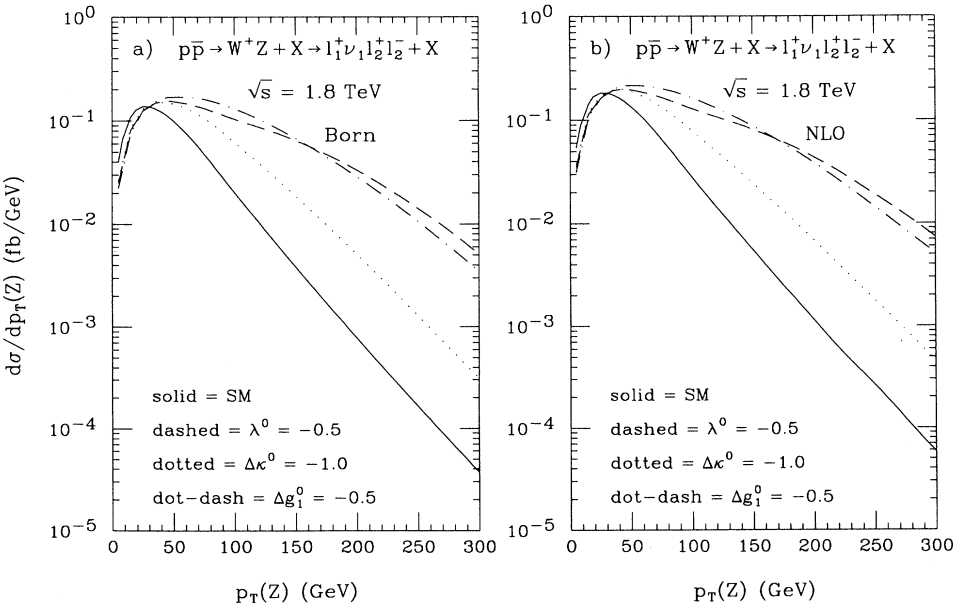

FIG. 7. The inclusive differential cross section for the transverse momentum of the Z boson in the reaction $p\bar{p} \to W^+Z + X \to \ell_1^+\nu_1\ell_2^+\ell_2^- + X$ at $\sqrt{s} = 1.8$ TeV (a) in the Born approximation and (b) including $O(\alpha_s)$ QCD corrections. The curves are for the SM (solid lines), $\lambda^0 = -0.5$ (dashed lines), $\Delta\kappa^0 = -1.0$ (dotted lines), and $\Delta g_1^0 = -0.5$ (dot-dashed lines). The cuts imposed are summarized in Sec. III B.

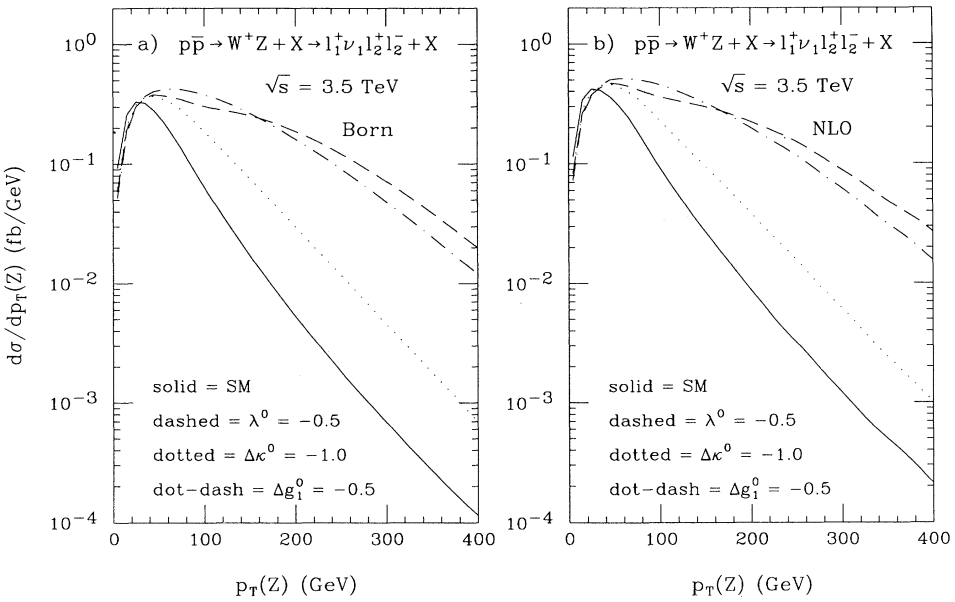

FIG. 8. The inclusive differential cross section for the transverse momentum of the Z boson in the reaction $p\bar{p} \to W^+Z+X \to \ell_1^+\nu_1\ell_2^+\ell_2^- + X$ at $\sqrt{s} = 3.5$ TeV (a) in the Born approximation and (b) including $O(\alpha_s)$ QCD corrections. The curves are for the SM (solid lines), $\lambda^0 = -0.5$ (dashed lines), $\Delta\kappa^0 = -1.0$ (dotted lines), and $\Delta g_1^0 = -0.5$ (dot-dashed lines). The cuts imposed are summarized in Sec. III B.

tive to nonstandard WWZ couplings than the cluster transverse mass or the WZ invariant mass distributions. At high transverse momentum, a large enhancement of the cross section is observed. On the other hand, at Tevatron and DiTevatron energies, the $p_T(Z)$ differential cross section is smaller than predicted in the SM for $p_T(Z) < 30$ GeV, if anomalous WWZ couplings are present. Due to the relatively large $\not{p}_T$ cut imposed, the Z boson transverse momentum distribution at the LHC in the Born approximation displays a pronounced shoulder at $p_T(Z) \approx 65$ GeV [see Fig. 9(a)]. The $\not{p}_T$ cut mostly affects the small $p_T(Z)$ region [$p_T(Z) < 100$ GeV] and therefore does not significantly reduce the sensitivity to nonstandard WWZ couplings. Once $O(\alpha_s)$ QCD corrections are taken into account, this shoulder disappears due to contributions from the real emission subprocesses $q_1\bar{q}_2 \to WZg$ and $q_1 g \to WZq_2$.

In contrast to the other distributions studied so far, the shape of the SM Z boson transverse momentum spectrum is considerably affected by $O(\alpha_s)$ QCD corrections. This is demonstrated in detail in Fig. 10, where we show the ratio of the NLO and LO differential cross sections of the Z boson transverse momentum. At Tevatron and DiTevatron energies, the $O(\alpha_s)$ corrections are approximately 30% for the SM, and 35–40% for the anomalous coupling cases at small $p_T(Z)$ values. In the SM case,

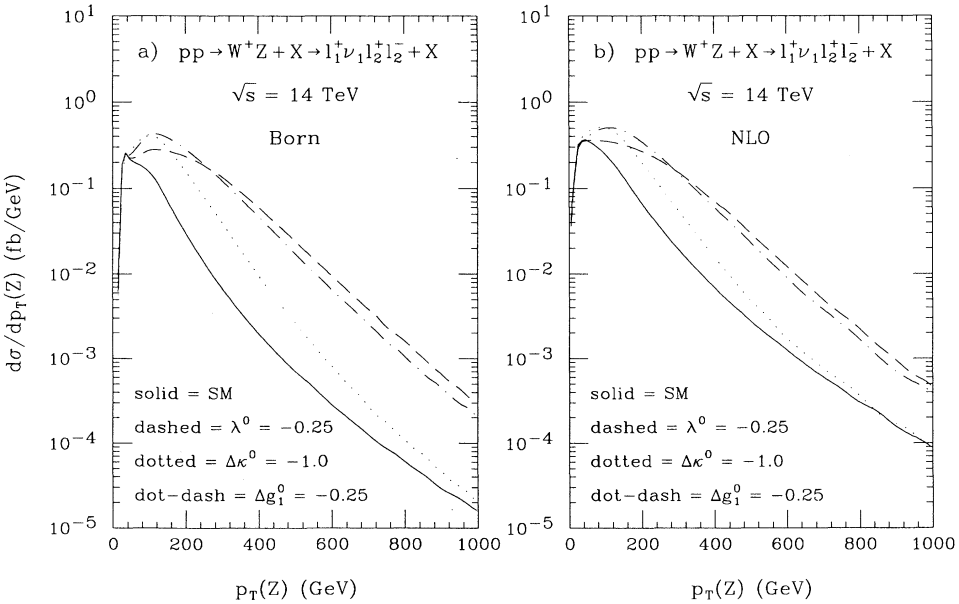

FIG. 9. The inclusive differential cross section for the transverse momentum of the Z boson in the reaction $pp \to W^+Z+X \to \ell_1^+\nu_1\ell_2^+\ell_2^- + X$ at $\sqrt{s} = 14$ TeV (a) in the Born approximation and (b) including $O(\alpha_s)$ QCD corrections. The curves are for the SM (solid lines), $\lambda^0 = -0.25$ (dashed lines), $\Delta\kappa^0 = -1.0$ (dotted lines), and $\Delta g_1^0 = -0.25$ (dot-dashed lines). The cuts imposed are summarized in Sec. III B.

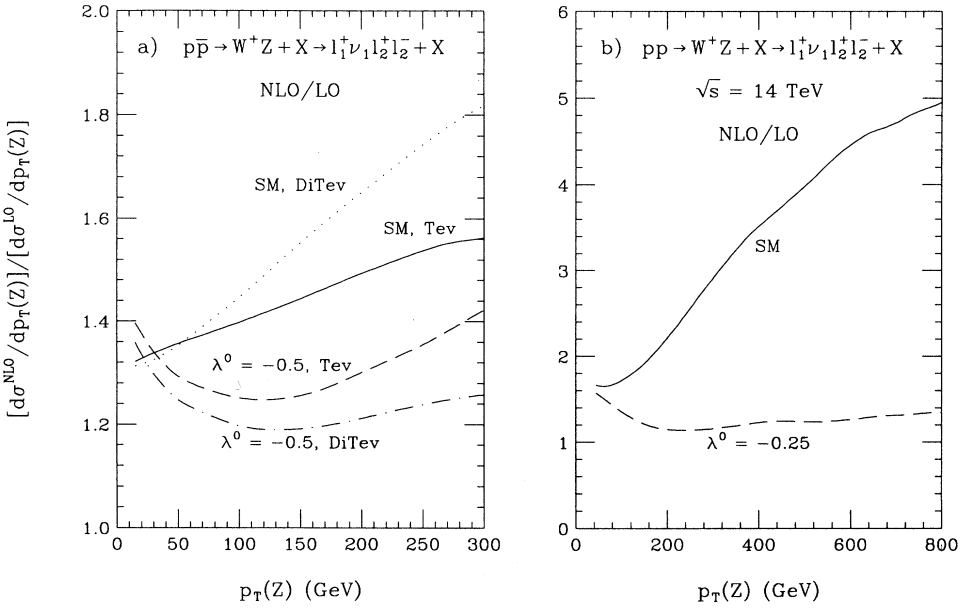

FIG. 10. Ratio of the NLO to LO differential cross sections of the Z boson transverse momentum as a function of $p_T(Z)$ for (a) $p\bar{p} \to W^+Z + X \to \ell_1^+\nu_1\ell_2^+\ell_2^- + X$ and (b) $pp \to W^+Z + X \to \ell_1^+\nu_1\ell_2^+\ell_2^- + X$ at $\sqrt{s} = 14$ TeV. In part (a) the solid (dotted) and dashed (dot-dashed) lines give the ratio in the SM and for $\lambda^0 = -0.5$ at the Tevatron (DiTevatron), respectively. In part (b) the solid and dashed curves show the ratio for the SM and $\lambda^0 = -0.25$ at the LHC. The cuts imposed are summarized in Sec. III B.

the size of the QCD corrections increases to $\sim 60\%$ for $p_T(Z) = 300$ GeV at the Tevatron, and to $\sim 80\%$ at the DiTevatron. For nonstandard couplings, on the other hand, the QCD corrections are between 20% and 40% over the whole $p_T(Z)$ range plotted. This is exemplified by the dashed and dot-dashed lines in Fig. 10(a), which show the ratio of NLO to LO cross sections for $\lambda^0 = -0.5$ at the Tevatron and DiTevatron, respectively. At the LHC [see Fig. 10(b)], the shape of the $p_T(Z)$ distribution is drastically altered by the $O(\alpha_s)$ QCD corrections. At $p_T(Z) = 800$ GeV, the QCD corrections increase the SM cross section by about a factor 5, whereas the enhancement is only a factor 1.6 at $p_T(Z) = 100$ GeV. In the presence of anomalous couplings, the higher order QCD corrections are much smaller than in the SM. In regions where the anomalous terms dominate, the $O(\alpha_s)$ corrections are typically between 20% and 40%. This is illustrated by the dashed curve in Fig. 10(b), which shows the NLO-to-LO cross section ratio for $\lambda^0 = -0.25$. At next-to-leading-order, the sensitivity of the Z boson transverse momentum spectrum to anomalous couplings is thus considerably reduced. The transverse momentum distribution of the W boson in the SM exhibits a similar strong sensitivity to QCD corrections. Qualitatively, the changes of the shape of the $p_T(Z)$ distribution in WZ production and of the photon transverse momentum distribution in $W\gamma$ production at high energies [49] are very similar.

E. Exclusive NLO cross sections

The large QCD corrections at high values of $p_T(Z)$ are caused by the combined effects of destructive interference in the Born process, a collinear enhancement factor in the $q_1 g \to WZq_2$ partonic cross section for $p_T(Z) \gg M_W$, and the large qg luminosity at LHC energies. In the SM, delicate cancellations between the amplitudes of the Born diagrams occur in the central rapidity region in WZ production. These cancellations are responsible for the approximate amplitude zero [5] and suppress the WZ differential cross section, in particular for large W and Z transverse momenta. In the limit $p_T(Z) \gg M_W$, the cross section for $q_1 g \to WZq_2$ can be obtained using the Altarelli-Parisi approximation for collinear emission. One finds [11]

$$d\hat{\sigma}(q_1 g \to WZq_2) = d\hat{\sigma}(q_1 g \to q_1 Z)\,\frac{g_W^2}{16\pi^2}\,\ln^2\left(\frac{p_T^2(Z)}{M_W^2}\right), \tag{12}$$

where $g_W = e/\sin\theta_W$. Thus, the quark gluon fusion process carries an enhancement factor $\ln^2[p_T^2(Z)/M_W^2]$ at large values of the Z boson transverse momentum. It arises from the kinematic region where the Z boson is produced at large p_T and recoils against the quark, which radiates a soft W boson collinear to the quark. Since the Feynman diagrams entering the derivation of Eq. (12) do not involve the WWZ vertex, the logarithmic enhancement factor only affects the SM matrix elements. At the LHC, the $p_T(Z)$ differential cross section obtained using Eq. (12) agrees within 30% with the exact Z boson transverse momentum distribution for $p_T(Z) > 200$ GeV [11]. Together with the very large qg luminosity at supercollider energies and the suppression of the SM WZ rate at large values of the Z boson transverse momentum in the Born approximation, the logarithmic enhancement factor is responsible for the size of the inclusive $O(\alpha_s)$ QCD corrections to WZ production, as well as for the change in the shape of the $p_T(Z)$ distribution. The same enhancement factor also appears in the antiquark gluon fusion process; however, the $\bar{q}g$ luminosity is much smaller than the qg luminosity for large values of the Z boson trans-

verse momentum. Since the W boson does not couple directly to the gluon, the process $q_1\bar{q}_2 \to WZg$ is not enhanced at large values of the Z boson transverse momentum. Arguments similar to those presented above also apply to the W boson transverse momentum distribution in the limit $p_T(W) \gg M_Z$, and a relation analogous to Eq. (12) can be derived.

From the picture outlined in the previous paragraph, one expects that, at next-to-leading order at supercollider energies, WZ events with a high p_T Z boson most of the time also contain a high transverse momentum jet. At the Tevatron, on the other hand, the fraction of high $p_T(Z)$ WZ events with a hard jet should be considerably smaller, due to the much smaller qg luminosity at lower energies. The decomposition of the inclusive SM NLO $p_T(Z)$ differential cross section into NLO 0-jet and LO 1-jet exclusive cross sections at the Tevatron and LHC is shown in Figs. 11(a) and 12(a), respectively. The SM NLO 0-jet $p_T(Z)$ distributions at the two center-of-mass energies are compared with the corresponding distributions obtained in the Born approximation in Figs. 11(b) and 12(b). Here, a jet is defined as a quark or gluon with

$$p_T(j) > 10 \text{ GeV} \qquad \text{and} \qquad |\eta(j)| < 2.5 \qquad (13)$$

at the Tevatron and

$$p_T(j) > 50 \text{ GeV} \qquad \text{and} \qquad |\eta(j)| < 3 \qquad (14)$$

at the LHC. The sum of the NLO 0-jet and the LO 1-jet exclusive cross sections is equal to the inclusive NLO cross section. The results for the NLO exclusive $WZ + 0$ jet and the LO exclusive $WZ + 1$ jet differential cross sections depend explicitly on the jet definition. Only the inclusive NLO distributions are independent of the jet definition. It should be noted that the jet transverse momentum threshold cannot be lowered to arbitrarily small values in our calculation for theoretical reasons. For transverse momenta below 5 GeV (20 GeV) at the Tevatron (LHC), soft gluon resummation effects are expected to significantly change the jet p_T distribution [50]. For the jet definitions listed above [Eqs. (13) and (14)], these effects are expected to be unimportant, and therefore are ignored in our calculation.

With the jet definition of Eq. (13), the inclusive NLO cross section at the Tevatron is composed predominately of 0-jet events [see Fig. 11(a)]. Because of the logarithmic enhancement factor, the 1-jet cross section becomes relatively more important at large values of the Z boson transverse momentum. For $p_T(Z)$ values above 200 GeV, the 1-jet cross section is larger than the 0-jet rate at the LHC, and dominates completely at high $p_T(Z)$ [see Fig. 12(a)]. Figure 11(b) compares the NLO $WZ + 0$ jet cross section with the result obtained in the Born approximation at the Tevatron. For the jet definition chosen [see Eq. (13)], the results are almost identical over the entire transverse momentum range displayed. At the LHC, the NLO $WZ + 0$ jet result is at most 20% smaller than the cross section obtained in the Born approximation [Fig. 12(b)]. Note that the characteristic shoulder at $p_T(Z) \approx 65$ GeV in the Born $p_T(Z)$ distribution, which results from the large $\not{p}_T$ cut, is eliminated in the NLO $WZ + 0$ jet differential cross section. The LO and NLO $WZ + 0$ jet $p_T(\ell_{1,2})$, $\not{p}_T$, and $y(\ell_{1,2})$ differential cross sections also agree to better than 20% [15]. The results for DiTevatron energies are very similar to those obtained for the Tevatron.

If the jet-defining p_T threshold is lowered to 30 GeV and jets can be identified out to $|\eta(j)| = 4.5$ at the LHC, the NLO $WZ + 0$ jet $p_T(Z)$ differential cross section is approximately 30% smaller than the result obtained with the jet definition of Eq. (14). Present stud-

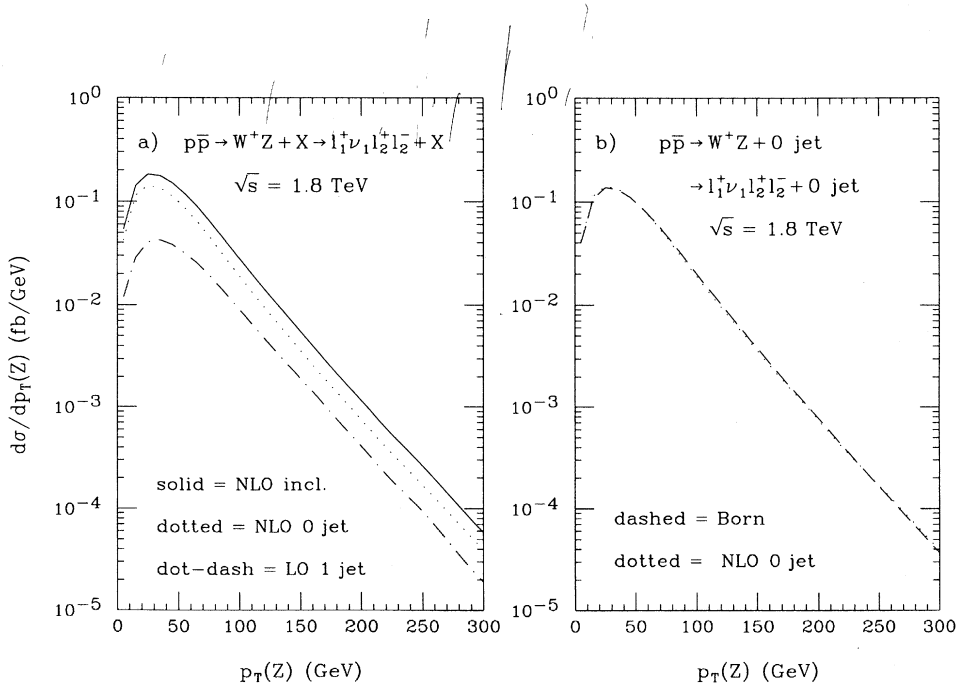

FIG. 11. The differential cross section for the Z boson transverse momentum in the reaction $p\bar{p} \to W^+Z + X \to \ell_1^+\nu_1\ell_2^+\ell_2^- + X$ at $\sqrt{s}$ = 1.8 TeV in the SM. (a) The inclusive NLO differential cross section (solid line) is shown, together with the $O(\alpha_s)$ 0-jet (dotted line) and the (LO) 1-jet (dot-dashed line) exclusive differential cross sections, using the jet definition in Eq. (13). (b) The NLO $WZ + 0$ jet exclusive differential cross section (dotted line) is compared with the Born differential cross section (dashed line). The cuts imposed are summarized in Sec. III B.

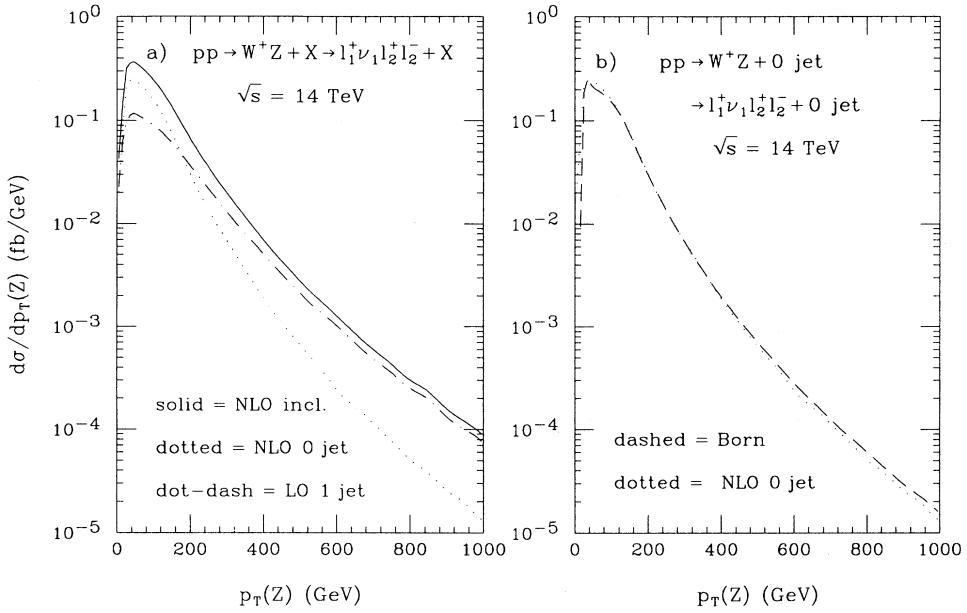

FIG. 12. The differential cross section for the Z boson transverse momentum in the reaction $pp \to W^+Z + X \to \ell_1^+\nu_1\ell_2^+\ell_2^- + X$ at $\sqrt{s}$ = 14 TeV in the SM. (a) The inclusive NLO differential cross section (solid line) is shown, together with the $O(\alpha_s)$ 0-jet (dotted line) and the (LO) 1-jet (dot-dashed line) exclusive differential cross sections, using the jet definition in Eq. (14). (b) The NLO $WZ + 0$ jet exclusive differential cross section (dotted line) is compared with the Born differential cross section (dashed line). The cuts imposed are summarized in Sec. III B.

ies suggest [43,44,51] that jets fulfilling the criteria of Eq. (14) can be identified at the LHC without problems, whereas it will be difficult to reconstruct a jet with a transverse momentum of less than 30 GeV. The pseudorapidity range covered by the LHC is not expected to extend beyond $|\eta| = 4.5$.

The results shown so far were obtained for $Q^2 = M_{WZ}^2$. Since the $WZ + 1$ jet and the $WZ + 0$ jet cross sections in the Born approximation are tree level results, they are sensitive to the choice of the factorization scale Q^2. Figure 13 displays the scale dependence of the Born, the inclusive NLO, the $O(\alpha_s)$ 0-jet exclusive, and the 1-jet exclusive cross sections for the Tevatron and LHC center-of-mass energies. The total cross section for the reaction $p\overset{(-)}{p} \to W^+Z + X \to \ell_1^+\nu_1\ell_2^+\ell_2^- + X$ is plotted versus the scale Q. The factorization scale M^2 and the renormalization scale μ^2 have both been set equal to Q^2.

The scale dependence of the Born cross section enters only through the Q^2 dependence of the parton distribution functions. The qualitative differences between the results at the Tevatron and the LHC are due to the differences between $p\bar{p}$ versus pp scattering and the ranges of the x values probed. At the Tevatron, WZ production in $p\bar{p}$ collisions is dominated by valence quark interactions. The valence quark distributions decrease with Q^2 for the

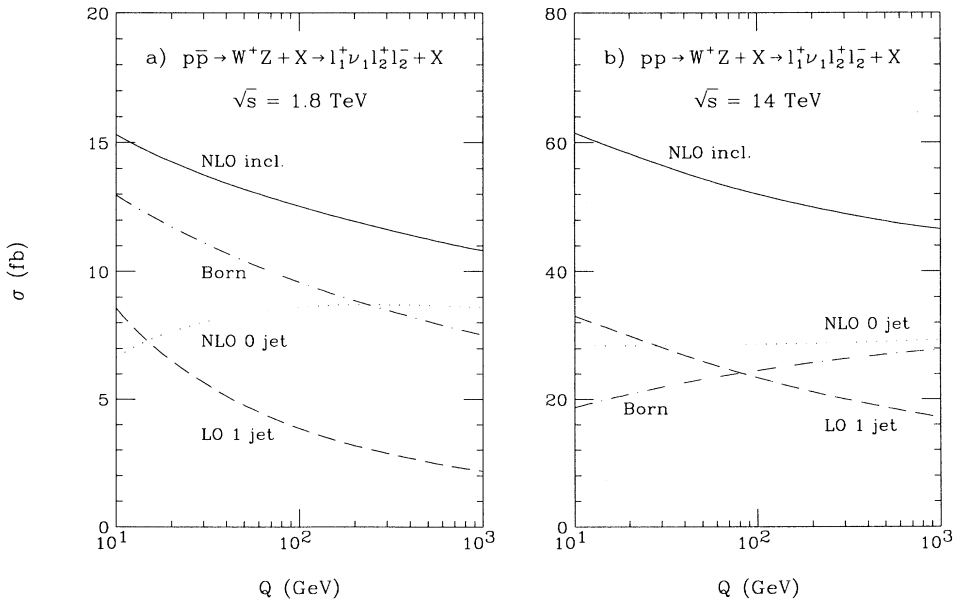

FIG. 13. The total cross section for $p\overset{(-)}{p} \to W^+Z + X \to \ell_1^+\nu_1\ell_2^+\ell_2^- + X$ in the SM versus the scale Q (a) at the Tevatron and (b) at the LHC. The curves represent the inclusive NLO (solid lines), the Born (dot-dashed lines), the LO 1-jet exclusive (dashed lines), and the NLO 0-jet exclusive (dotted lines) cross sections. The cuts imposed are summarized in Sec. III B. For the jet definitions, we have used Eqs. (13) and (14).

x values probed at the Tevatron (typically $x > 0.1$). On the other hand, at the LHC, sea quark interactions dominate in the pp process and smaller x values are probed (typically $x \sim 0.02$). The sea quark distributions increase with Q^2 for the x values probed at the LHC. Thus the Born cross section decreases with Q^2 at the Tevatron but increases with Q^2 at the LHC.

The scale dependence of the 1-jet exclusive cross section enters via the parton distribution functions and the running coupling $\alpha_s(Q^2)$. Note that the 1-jet exclusive cross section is calculated only to lowest order and thus exhibits a strong scale dependence. The dependence on Q here is dominated by the scale dependence of $\alpha_s(Q^2)$ which is a decreasing function of Q^2. At the NLO level, the Q dependence enters not only via the parton distribution functions and the running coupling $\alpha_s(Q^2)$, but also through explicit factorization scale dependence in the order $\alpha_s(Q^2)$ correction terms. The NLO 0-jet exclusive cross section is almost independent of the scale Q. It shows a non-negligible variation with the scale only in the region $Q < 100$ GeV at the Tevatron. In the $WZ + 0$ jet cross section, the scale dependence of the parton distribution functions is compensated by that of $\alpha_s(Q^2)$ and the explicit factorization scale dependence in the correction terms. The Q dependence of the inclusive NLO cross section is dominated by the 1-jet exclusive component and is significantly larger than that of the NLO 0-jet cross section.

F. Sensitivity limits

We now study the impact that $O(\alpha_s)$ QCD corrections to WZ production have on the sensitivity limits for Δg_1^0, $\Delta\kappa^0$, and λ^0 at the Tevatron, DiTevatron, and LHC. For the Tevatron we consider integrated luminosities of $\int \mathcal{L} dt = 1$ fb^{-1}, as envisioned for the main injector era, and 10 fb^{-1} (TeV*) which could be achieved through additional upgrades of the Tevatron accelerator complex [8]. In the case of the DiTevatron we assume an integrated luminosity of 10 fb^{-1}. For the LHC we consider integrated luminosities of $\int \mathcal{L} dt = 10$ fb^{-1} and 100 fb^{-1} [9]. To extract limits at the Tevatron, TeV*, and DiTevatron, we shall sum over both W charges. For the LHC, we only consider W^+Z production. Interference effects between Δg_1^0, $\Delta\kappa^0$, and λ^0 are fully incorporated in our analysis.

To derive 95% C.L. limits we use the $p_T(Z)$ distribution and perform a χ^2 test [52]. In the Born approximation, the Z boson transverse momentum distribution in general yields the best sensitivity bounds. Furthermore, we use the cuts summarized in Sec. III B, and the jet definitions of Eqs. (13) and (14). Unless explicitly stated otherwise, a dipole form factor ($n = 2$) with scale $\Lambda_{\rm FF} = 1$ TeV is assumed. For the Tevatron with 1 fb^{-1} we split the $p_T(Z)$ distribution into three bins, whereas seven bins are used in all other cases. In each bin the Poisson statistics are approximated by a Gaussian distribution. In order to achieve a sizable count-

TABLE I. Sensitivities achievable at the 95% confidence level (C.L.) for the anomalous WWZ couplings Δg_1^0, $\Delta\kappa^0$, and λ^0 in $p\bar{p} \to W^\pm Z + X \to \ell_1^\pm \nu_1 \ell_2^+ \ell_2^- + X$ at (a) leading-order and (b) next-to-leading-order for the Tevatron, the TeV* ($\sqrt{s} = 1.8$ TeV in both cases), and the DiTevatron ($\sqrt{s} = 3.5$ TeV). The limits for each coupling apply for arbitrary values of the two other couplings. For the form factors we use Eqs. (7), (8), and (9) with $n = 2$ and $\Lambda_{\rm FF} = 1$ TeV. The cuts summarized in Sec. III B are imposed.

(a) Leading-order

	Tevatron	TeV*	DiTevatron
Coupling	$\int \mathcal{L} dt = 1$ fb^{-1}	$\int \mathcal{L} dt = 10$ fb^{-1}	$\int \mathcal{L} dt = 10$ fb^{-1}
Δg_1^0	$+0.52$	$+0.26$	$+0.15$
	-0.29	-0.10	-0.05
$\Delta\kappa^0$	$+1.9$	$+1.0$	$+0.5$
	-1.4	-0.7	-0.5
λ^0	$+0.34$	$+0.15$	$+0.08$
	-0.37	-0.15	-0.07

(b) Next-to-leading-order

Δg_1^0	$+0.50$	$+0.25$	$+0.15$
	-0.27	-0.10	-0.05
$\Delta\kappa^0$	$+1.8$	$+1.0$	$+0.6$
	-1.2	-0.7	-0.5
λ^0	$+0.33$	$+0.15$	$+0.08$
	-0.34	-0.14	-0.08

ing rate in each bin, all events with $p_T(Z) > 60$ GeV (120 GeV) at the Tevatron (TeV*) are collected in a single bin. Similarly, all events with $p_T(Z) > 180$ GeV (240 GeV [480 GeV]) at the DiTevatron (LHC with 10 fb^{-1} [100 fb^{-1}]) are accumulated into one bin. This procedure guarantees that a high statistical significance cannot arise from a single event at large transverse momentum, where the SM predicts, say, only 0.01 events. In order to derive realistic limits we allow for a normalization uncertainty of 50% in the SM cross section. Background contributions are expected to be small for the cuts we impose, and are ignored in our derivation of sensitivity bounds.

Our results are summarized in Figs. 14 and 15, and Tables I and II. The cross section in each bin is a bilinear function of the anomalous couplings $\Delta\kappa^0$, λ^0, and

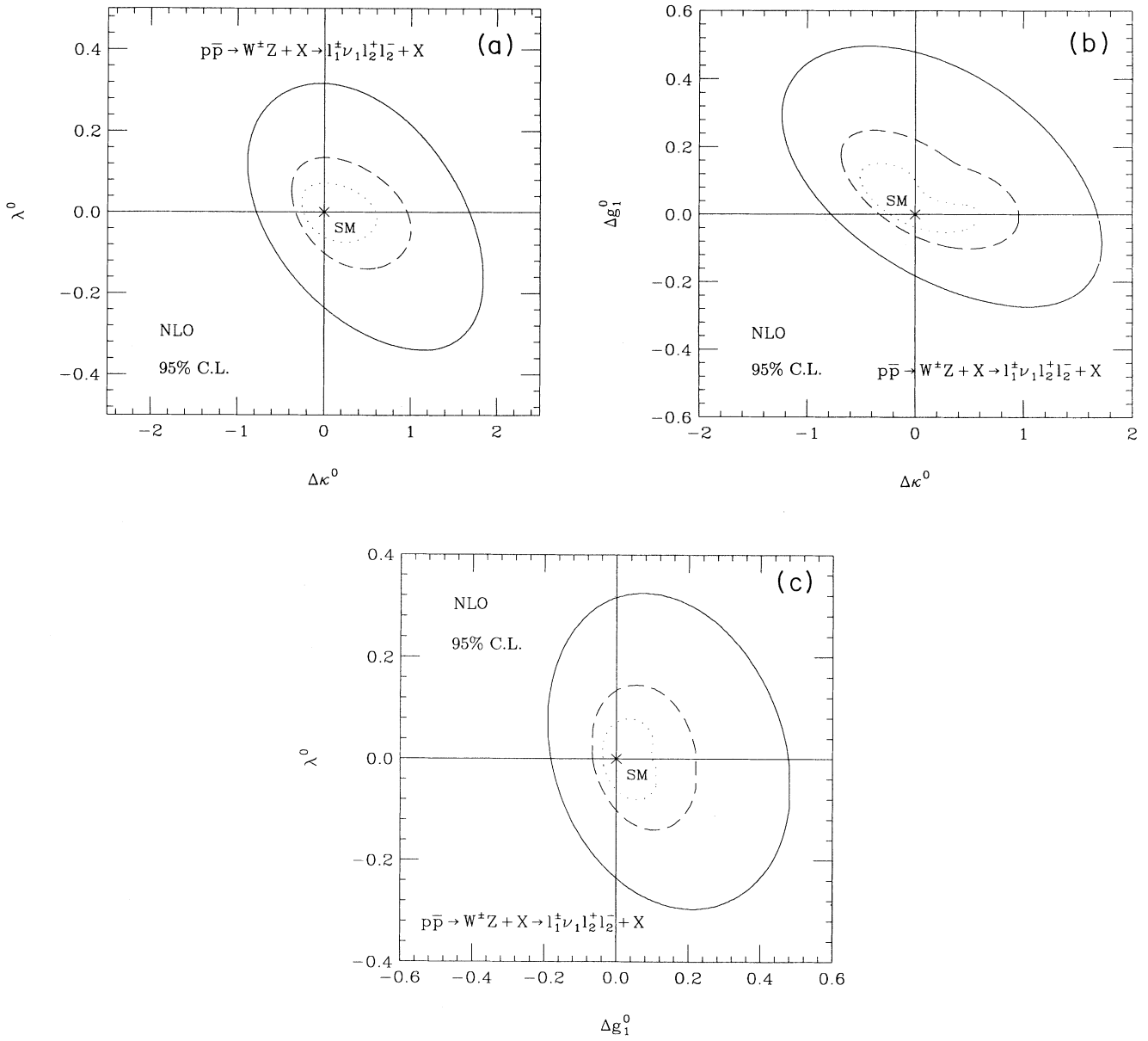

FIG. 14. Limit contours at the 95% C.L. for $p\bar{p} \to W^{\pm}Z + X \to \ell_1^{\pm}\nu_1\ell_2^{+}\ell_2^{-} + X$ derived from the inclusive NLO $p_T(Z)$ distribution. Contours are shown in three planes: (a) the $\Delta\kappa^0$-λ^0 plane, (b) the $\Delta\kappa^0$-Δg_1^0 plane, and (c) the Δg_1^0-λ^0 plane. The solid and dashed lines give the results for the Tevatron ($\sqrt{s} = 1.8$ TeV) with $\int \mathcal{L}dt = 1$ fb^{-1} and $\int \mathcal{L}dt = 10$ fb^{-1}, respectively. The dotted curve shows the result obtained for the DiTevatron ($\sqrt{s} = 3.5$ TeV) with $\int \mathcal{L}dt = 10$ fb^{-1}. The cuts imposed are summarized in Sec. III B.

Δg_1^0. Studying the correlations in the $\Delta\kappa^0$ – λ^0, the $\Delta\kappa^0$ – Δg_1^0, and the Δg_1^0 – λ^0 planes is therefore sufficient to fully include all interference effects between the various WWZ couplings. Figure 14 shows 95% C.L. contours in the three planes for the $p\bar{p}$ collider options obtained from the inclusive NLO $p_T(Z)$ distribution. Table I displays the 95% C.L. sensitivity limits, including all correlations, at leading order and next-to-leading order for the three WWZ couplings for the process $p\bar{p} \to W^{\pm}Z + X \to \ell_1^{\pm}\nu_1\ell_2^+\ell_2^- + X$. At Tevatron and DiTevatron energies, the increase of the cross section at $O(\alpha_s)$ and the reduced sensitivity at large values of the Z boson transverse momentum balance each other, and the limits obtained at LO and NLO are usually very similar. Our limits fully reflect the strong sign dependence of the differential cross sections observed for $\Delta\kappa^0$ and Δg_1^0 (see Fig. 5).

With an integrated luminosity of 1 fb^{-1} it will not

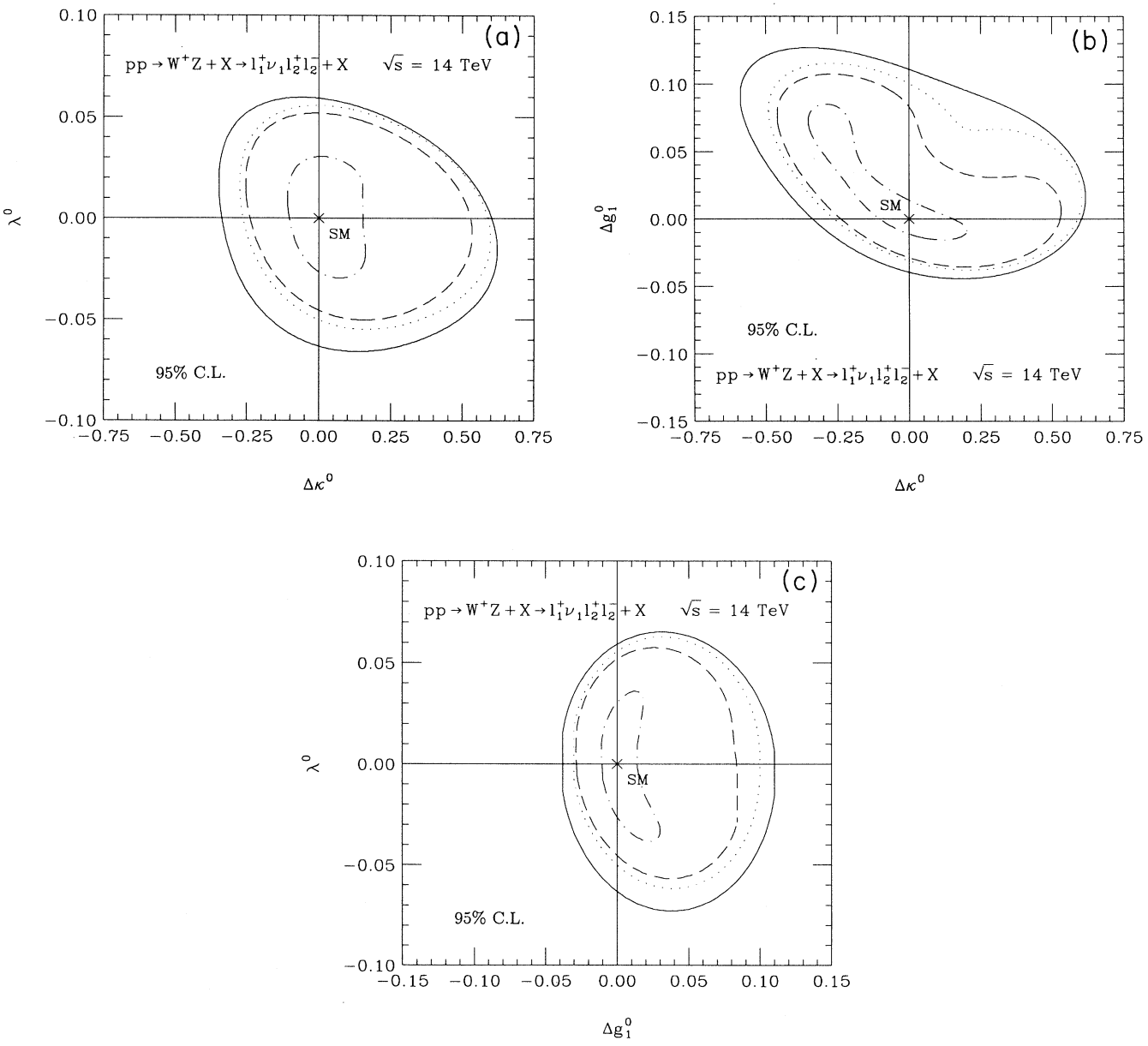

FIG. 15. Limit contours at the 95% C.L. for $pp \to W^+Z + X \to \ell_1^+\nu_1\ell_2^+\ell_2^- + X$ at $\sqrt{s} = 14$ TeV derived from the $p_T(Z)$ distribution. Contours are shown in three planes: (a) the $\Delta\kappa^0$-λ^0 plane, (b) the $\Delta\kappa^0$-Δg_1^0 plane, and (c) the Δg_1^0-λ^0 plane. The solid and dashed lines give the inclusive NLO and LO results, respectively, for $\int \mathcal{L}dt = 10$ fb^{-1}. The dotted and dot-dashed curves show the results obtained from the exclusive NLO $WZ+0$ jet channel for integrated luminosities of 10 fb^{-1} and 100 fb^{-1}, respectively. The cuts imposed are summarized in Sec. III B.

be possible to perform a very precise measurement of the WWZ vertex in the $WZ \to \ell_1\nu_1\ell_2^+\ell_2^-$ channel at the Tevatron. For integrated luminosities of less than a few fb^{-1}, the limits which can be achieved, however, may be significantly improved by combining the bounds from $WZ \to \ell_1\nu_1\ell_2^+\ell_2^-$ with the limits obtained from $p\bar{p} \to WZ \to \ell_1\nu_1 jj$ and $p\bar{p} \to WZ \to jj\ell_2^+\ell_2^-$ at large dijet transverse momenta [53]. Currently, these channels are used by the CDF Collaboration to extract information on the structure of the WWZ vertex [7,18]. Decay modes where the W or Z boson decays hadronically have a considerably larger branching ratio than the $WZ \to \ell_1\nu_1\ell_2^+\ell_2^-$ channel and thus yield higher rates. On the other hand, they are plagued by a substantial $W/Z+2$ jet QCD background, which, for large integrated luminosities (≥ 10 fb^{-1}), will eventually limit the sensitivity of the semihadronic WZ decay channels to anomalous WWZ couplings.

The limits which can be achieved for $\Delta\kappa^0$ at the TeV* from $WZ \to \ell_1\nu_1\ell_2^+\ell_2^-$ are about a factor 1.8 better than those at the Tevatron with 1 fb^{-1}. The bounds on Δg_1^0 and λ^0 improve by a factor of 2–2.7. Increasing the energy of the Tevatron to 3.5 TeV (DiTevatron) improves the limits again significantly, in particular, the bound on $\Delta\kappa^0$. Due to the rather strong interference effects between the SM and the anomalous terms of the helicity amplitudes for Δg_1 and $\Delta\kappa$, the contours sometimes deviate substantially from the elliptical form

TABLE II. Sensitivities achievable at the 95% confidence level (C.L.) for the anomalous WWZ couplings Δg_1^0, $\Delta\kappa^0$, and λ^0 in $pp \to W^+Z + X \to \ell_1^+\nu_1\ell_2^+\ell_2^- + X$ at the LHC ($\sqrt{s} = 14$ TeV). The limits for each coupling apply for arbitrary values of the two other couplings. For the form factors we use Eqs. (7), (8), and (9) with $n = 2$. The cuts summarized in Sec. III B are imposed. In the NLO 0-jet case we have used the jet definition of Eq. (14).

Coupling	Born appr.	incl. NLO	NLO 0-jet
(a) $\int \mathcal{L}dt = 10$ fb^{-1}, $\Lambda_{\rm FF} = 1$ TeV			
Δg_1^0	$+0.108$ -0.036	$+0.127$ -0.044	$+0.115$ -0.038
$\Delta\kappa^0$	$+0.53$ -0.46	$+0.62$ -0.59	$+0.60$ -0.49
λ^0	$+0.058$ -0.057	$+0.065$ -0.073	$+0.063$ -0.062
(b) $\int \mathcal{L}dt = 100$ fb^{-1}, $\Lambda_{\rm FF} = 1$ TeV			
Δg_1^0	$+0.082$ -0.014	$+0.096$ -0.018	$+0.085$ -0.016
$\Delta\kappa^0$	$+0.17$ -0.34	$+0.24$ -0.41	$+0.20$ -0.35
λ^0	$+0.038$ -0.036	$+0.042$ -0.048	$+0.036$ -0.038
(c) $\int \mathcal{L}dt = 100$ fb^{-1}, $\Lambda_{\rm FF} = 3$ TeV			
Δg_1^0	$+0.0164$ -0.0048	$+0.0200$ -0.0066	$+0.0188$ -0.0050
$\Delta\kappa^0$	$+0.092$ -0.120	$+0.128$ -0.160	$+0.108$ -0.132
λ^0	$+0.0084$ -0.0082	$+0.0102$ -0.0100	$+0.0092$ -0.0090

naively expected. Furthermore, significant correlations are observed, in particular, between $\Delta\kappa^0$ and Δg_1^0 [see Fig. 14(b)]. The limits obtained with a 0-jet requirement imposed are virtually identical to those resulting from the inclusive NLO $p_T(Z)$ distribution.

The 95% C.L. limit contours for the LHC are shown in Fig. 15. Table II summarizes the LO and NLO sensitivity bounds which can be achieved at the LHC. At supercollider energies, the inclusive $O(\alpha_s)$ QCD corrections in the SM are very large and drastically change the shape of the SM $p_T(Z)$ distribution (see Fig. 9). As a result, $O(\alpha_s)$ QCD corrections reduce the sensitivity to anomalous couplings by 20–40%. As the integrated luminosity increases, larger transverse momenta become accessible. The difference between the LO and NLO sensitivity bounds for 100 fb^{-1} therefore is somewhat larger than for 10 fb^{-1}. For the parameters chosen, the inclusive NLO bounds which can be obtained from $pp \to W^+Z + X \to \ell_1^+\nu_1\ell_2^+\ell_2^- + X$ at $\sqrt{s} = 14$ TeV with $\int \mathcal{L}dt = 10$ fb^{-1} are quite similar to those which are expected from the DiTevatron for $W^\pm Z$ production and equal integrated luminosity.

As we have seen in Sec. III E, the size of the $O(\alpha_s)$ QCD corrections at the LHC can be significantly reduced by vetoing hard jets in the central rapidity region, i.e., by imposing a "zero jet" requirement and considering only the $WZ+0$ jet channel. A 0-jet cut for example has been imposed in the CDF measurement of the ratio of W to Z cross sections [54] and the W mass measurement [55]. The sensitivity limits obtained for the $WZ + 0$ jet channel at NLO are 10–30% better than those obtained in the inclusive NLO case and are quite often close to those obtained from the leading-order $p_T(Z)$ distribution (see Table II and the dotted contours in Fig. 15). The NLO $WZ + 0$ jet differential cross section is also more stable to variations of the factorization scale Q^2 than the Born and inclusive NLO $WZ + X$ cross sections (see Fig. 13). The systematic errors which originate from the choice of Q^2 will thus be smaller for bounds derived from the NLO $WZ + 0$ jet differential cross section than those obtained from the inclusive NLO $WZ + X$ or the Born cross section. The limits extracted from the $WZ + 0$ jet exclusive channel depend only negligibly on the jet definition used.

The bounds which can be achieved at the LHC improve by up to a factor 3 if an integrated luminosity of 100 fb^{-1} can be achieved (dot-dashed contours in Fig. 15). Note that the $\Delta\kappa^0$ and Δg_1^0 limits are strongly correlated in this case. This effect is due to the relatively small form factor scale chosen ($\Lambda_{\rm FF} = 1$ TeV), which significantly suppresses the nonstandard terms in the helicity amplitudes at high energies.

At Tevatron (DiTevatron) energies, the sensitivities achievable are insensitive to the exact form and scale of the form factor for $\Lambda_{\rm FF} > 400$ GeV ($\Lambda_{\rm FF} > 800$ GeV). At the LHC, the situation is somewhat different and the sensitivity bounds depend on the value chosen for $\Lambda_{\rm FF}$ [3]. This is illustrated in Table II(c), where we list the bounds which can be achieved at the LHC with $\int \mathcal{L}dt = 100$ fb^{-1} and a form factor scale of $\Lambda_{\rm FF} = 3$ TeV. The limits for the higher scale are a factor 1.8–5 better than those found for $\Lambda_{\rm FF} = 1$ TeV with the same integrated luminosity. For $\Lambda_{\rm FF} > 3$ TeV, the sensitivity bounds depend only marginally on the form factor scale, due to the very rapidly falling cross section at the LHC for parton center-of-mass energies in the multi-TeV region. The dependence of the limits on the cutoff scale $\Lambda_{\rm FF}$ in the form factor can be understood easily from Fig. 9. The improvement in sensitivity with increasing $\Lambda_{\rm FF}$ is due to the additional events at large $p_T(Z)$ which are suppressed by the form factor if the scale $\Lambda_{\rm FF}$ has a smaller value.

To a lesser degree, the bounds also depend on the power n in the form factor, which we have assumed to be $n = 2$. For example, the less drastic cutoff for $n = 1$ instead of $n = 2$ in the form factor allows for additional high $p_T(Z)$ events and therefore leads to a slightly increased sensitivity to the low energy values $\Delta\kappa^0$, Δg_1^0, and λ^0. The sensitivity bounds listed in Tables I and II can thus be taken as representative for a wide class of form factors, including the case where constant anomalous couplings are assumed for $M_{WZ} < \Lambda_{\rm FF}$, but invariant masses above $\Lambda_{\rm FF}$ are ignored in deriving the sensitivity bounds [26].

The bounds derived in this section are quite conservative. At the LHC, the limits can easily be improved by 10–20% if $W^-Z + X$ production is included. Further improvements may result from using more powerful statistical tools than the simple χ^2 test we performed [56].

IV. AMPLITUDE ZEROS, RAPIDITY CORRELATIONS, AND CROSS SECTION RATIOS

Recently, it has been shown that the SM amplitude for $q_1\bar{q}_2 \to W^\pm Z$ at the Born level exhibits an approximate zero at high energies, $\hat{s} \gg M_Z^2$, located at [5]

$$\cos\Theta^* = \cos\Theta_0^* \approx \pm\frac{1}{3}\tan^2\theta_{\rm W} \approx \pm 0.1, \tag{15}$$

where Θ^* is the scattering angle of the Z boson relative to the quark direction in the WZ center-of-mass frame. The approximate zero is the combined result of an exact zero in the dominant helicity amplitudes $\mathcal{M}(\pm,\mp)$, and strong gauge cancellations in the remaining amplitudes. At high energies, only the $(\pm,\mp)$ and $(0,0)$ amplitudes remain nonzero in the SM. The existence of the zero in $\mathcal{M}(\pm,\mp)$ at $\cos\Theta^* \approx \pm 0.1$ is a direct consequence of the contributing u- and t-channel fermion exchange diagrams and the left-handed coupling of the W boson to fermions. Unlike the $W^\pm\gamma$ case with its massless photon kinematics, the zero has an energy dependence which is, however, rather weak for energies sufficiently above the WZ mass threshold.

In this section, we consider possible observable consequences of the approximate zero in WZ production in hadronic collisions and the impact of $O(\alpha_s)$ QCD corrections on the relevant quantities. All numerical simulations are carried out using the parameters and cuts summarized in Secs. III A and III B. For the form factor, we again assume a dipole form factor ($n = 2$) with scale $\Lambda_{\rm FF} = 1$ TeV [see Eqs. (7)–(9)]. Since the approximate amplitude zero in WZ production is similar in nature to

the well-known radiation zero in $W\gamma$ production, analogous strategies can be applied to search for observable signals. The radiation zero in $W\gamma$ production leads to a pronounced dip in the rapidity distribution of the photon in the parton center-of-mass frame, $d\sigma/dy^*(\gamma)$ [31]. The approximate zero in the WZ amplitude is therefore expected to manifest itself as a dip in the corresponding $y^*(Z)$ distribution. Here,

$$y^*(Z) = \frac{1}{2} \ln\left(\frac{1+\beta_Z \cos\theta^*}{1-\beta_Z \cos\theta^*}\right) \tag{16}$$

and

$$\beta_Z = \left[1 - \frac{4M_Z^2 \hat{s}}{(\hat{s} - M_W^2 + M_Z^2)^2}\right]^{1/2}, \tag{17}$$

where, to lowest order, $\hat{s} = M_{WZ}^2$ is the squared parton center-of-mass energy, and θ^* the scattering angle of the Z boson with respect to the beam direction in the parton center-of-mass rest frame. For pp collisions the dip is centered at $y^*(Z) = 0$. In $p\bar{p}$ collisions, the location of the minimum is determined by $\cos\Theta_0^*$ of Eq. (15), the average WZ invariant mass, and the fraction of events originating from sea quark collisions. As can be seen from Figs. 2 and 3, most of the cross section originates from the region $\sqrt{\hat{s}} = 200$–250 GeV. Valence quark collisions dominate at both, Tevatron and DiTevatron energies. The minimum of the $y^*(Z)$ distribution is therefore expected to occur at $y^*(Z) \approx \pm 0.06$.

The $|y^*(Z)|$ distribution at the Tevatron and the LHC in Born approximation is shown in Fig. 16. The rapidity distribution of the Z boson in the parton center-of-mass frame at the DiTevatron is qualitatively very similar to that found at Tevatron energies and is therefore not shown. The SM $|y^*(Z)|$ distribution in the true WZ rest frame (double-dotted-dashed curves) displays a pronounced dip at $|y^*(Z)| = 0$, which originates from the approximate amplitude zero. At Tevatron energies, the dip is quite significant. However, since the unobservable longitudinal neutrino momentum can only be determined with a twofold ambiguity and, on an event-by-event basis, one does not know which solution is the correct one, both solutions have to be considered for each event. Assigning half of the event weight to each solution, the dip in the $|y^*(Z)|$ distribution using the reconstructed WZ rest frame is considerably filled in (solid lines). $O(\alpha_s)$ QCD corrections further diminish the significance of the dip.

In Fig. 16 we also display the effect of nonstandard WWZ couplings on the $|y^*(Z)|$ distribution (using the reconstructed WZ rest frame). The lower dotted, dashed, and dot-dashed lines display the $|y^*(Z)|$ distribution for $\Delta\kappa^0 = +1$ $(+1)$, $\Delta g_1^0 = +0.5$ $(+0.25)$, and $\lambda^0 = +0.5$ $(+0.25)$, whereas the upper curves show the $|y^*(Z)|$ spectrum for $\Delta\kappa^0 = -1$ (-1), $\Delta g_1^0 = -0.5$ (-0.25), and $\lambda^0 = -0.5$ (-0.25) at the Tevatron (LHC). Nonstandard WWZ couplings eliminate the approximate amplitude zero [5] and, in general, tend to fill in the dip. However, because of the relatively strong interference between standard and anomalous contributions to the helicity amplitudes for $\Delta\kappa^0$ and Δg_1^0 at low energies, the dip may even become more pronounced for certain (positive) values of these two couplings at the Tevatron [see the lower dotted line in Fig. 16(a)].

From Fig. 16 it is obvious that the dip signaling the approximate amplitude zero in $q_1\bar{q}_2 \to WZ$ will be difficult to observe in the $|y^*(Z)|$ distribution. In $W\gamma$ production, correlations between the rapidities of the photon and the charged lepton originating from the W decay offer better access to the SM radiation zero than the $y^*(\gamma)$ distribution [13]. Knowledge of the neutrino

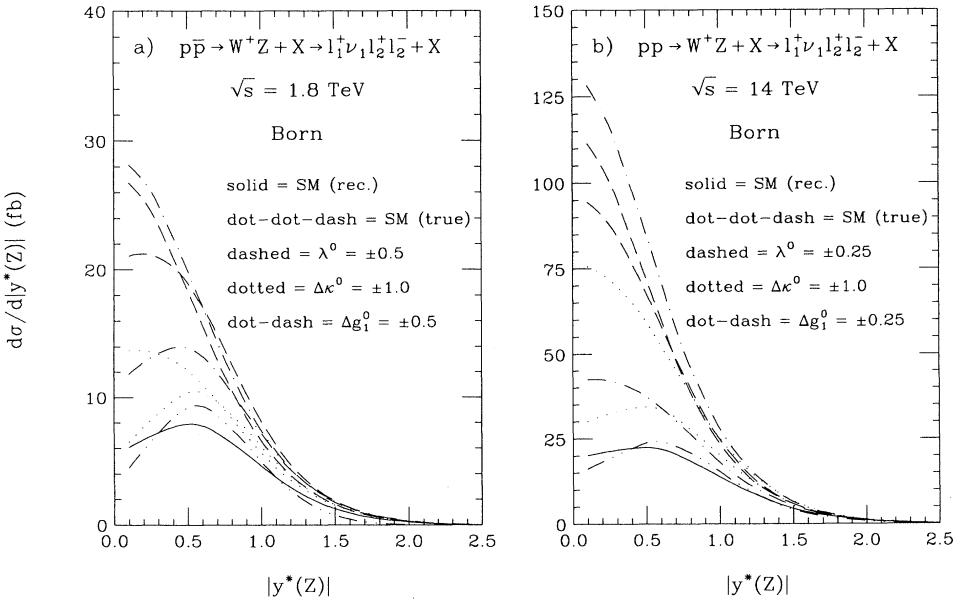

FIG. 16. Rapidity spectrum of the Z boson in the WZ rest frame in the Born approximation for (a) $p\bar{p} \to W^+Z + X \to \ell_1^+\nu_1\ell_2^+\ell_2^- + X$ at $\sqrt{s} = 1.8$ TeV and (b) $pp \to W^+Z + X \to \ell_1^+\nu_1\ell_2^+\ell_2^- + X$ at $\sqrt{s} = 14$ TeV. The curves are for the SM with reconstructed WZ rest frame (solid lines) and nonstandard WWZ couplings (dotted, dashed, and dot-dashed curves) as listed in the figure. The lower (upper) lines apply for positive (negative) anomalous couplings. The double-dotted-dashed line shows the true SM $|y^*(Z)|$ distribution. The cuts imposed are summarized in Sec. III B.

longitudinal momentum $p_L(\nu)$ is not required in determining these correlations, and thus event reconstruction problems originating from the two possible solutions for $p_L(\nu)$ are automatically avoided. In $2 \to 2$ reactions rapidity differences are invariant under boosts, $\Delta y(\gamma, W) = y(\gamma) - y(W) = y^*(\gamma) - y^*(W)$. One therefore expects the rapidity difference distribution $d\sigma/d\Delta y(\gamma, W)$ to exhibit a dip signaling the SM radiation zero. In $W^{\pm}\gamma$ production, the dominant W helicity in the SM is $\lambda_W = \pm 1$ [57], implying that the charged lepton from $W \to \ell\nu$ tends to be emitted in the direction of the parent W, and thus reflects most of its kinematic properties. As a result, the dip signaling the SM radiation zero manifests itself also in the $\Delta y(\gamma, \ell) = y(\gamma) - y(\ell)$ distribution.

The corresponding $y(Z) - y(\ell_1)$ distribution for W^+Z production in the Born approximation is shown in Fig. 17 (solid line). Analogous to the situation encountered in $q_1\bar{q}_2 \to W\gamma$, the approximate zero in the WZ amplitude leads to a dip in the $y(Z) - y(W)$ distribution [11], which is located at $y(Z) - y(W) \approx \pm 0.12$ $(= 0)$ for $W^{\pm}Z$ production in $p\bar{p}$ (pp) collisions. However, in contrast to $W\gamma$ production, none of the W helicities dominates in WZ production [57]. The charged lepton ℓ_1, originating from the W decay $W \to \ell_1\nu_1$, thus only partly reflects the kinematical properties of the parent W boson. As a result, a significant part of the correlation present in the $y(Z) - y(W)$ spectrum is lost, and only a slight dip survives in the SM $y(Z) - y(\ell_1)$ distribution. Due to the nonzero average rapidity difference between the lepton ℓ_1 and the parent W boson, the location of the minimum of the $y(Z) - y(\ell_1)$ distribution in $p\bar{p}$ collisions is slightly shifted to $y(Z) - y(\ell_1) \approx 0.5$. The $y(Z) - y(\ell_1)$ distribution at the DiTevatron is qualitatively very similar to that obtained for $p\bar{p}$ collisions at $\sqrt{s} = 1.8$ TeV (see Fig. 18).

The significance of the dip in the $y(Z) - y(\ell_1)$ distribution depends to some extent on the cut imposed on $p_T(\ell_1)$ and the missing transverse momentum. Increasing (decreasing) the cut on $p_T(\ell_1)$ $(\not{p}_T)$ tends to increase the probability that ℓ_1 is emitted in the flight direction of the W boson, and thus enhances the significance of the dip. If the $\not{p}_T > 50$ GeV cut at the LHC could be reduced to 20 GeV, the dip signaling the approximate zero in the WZ production amplitude would be strengthened considerably.

Although the Z boson rapidity can readily be reconstructed from the four-momenta of the lepton pair $\ell_2^+\ell_2^-$ originating from the Z decay, it would be experimentally easier to directly study the rapidity correlations between the charged leptons originating from the $Z \to \ell_2^+\ell_2^-$ and $W \to \ell_1\nu_1$ decays. The dotted lines in Fig. 17 show the SM $y(\ell_2^-) - y(\ell_1^+)$ distribution for W^+Z production in the Born approximation. Because none of the Z or W helicities dominates [57] in $q_1\bar{q}_2 \to WZ$, the rapidities of the leptons from W and Z decays are almost completely uncorrelated, and essentially no trace of the dip signaling the approximate amplitude zero is left in the $y(\ell_2^-) - y(\ell_1^+)$ distribution. The $y(\ell_2^+) - y(\ell_1^+)$ spectrum almost coincides with the $y(\ell_2^-) - y(\ell_1^+)$ distribution and is therefore not shown.

In Figs. 18 and 19 we show the influence of $O(\alpha_s)$ QCD corrections and nonstandard WWZ couplings (at NLO) on the $\Delta y(Z, \ell_1) = y(Z) - y(\ell_1)$ spectrum. At Tevatron energies, the shape of the distribution is seen to be hardly influenced by the $O(\alpha_S)$ QCD corrections. At the DiTevatron, the significance of the dip is slightly reduced. At LHC energies, the dip is completely eliminated by the inclusive QCD corrections. The NLO $WZ + 0$ jet $\Delta y(Z, \ell_1)$ distribution, however, is very similar to the leading-order rapidity difference distribution [see Fig. 19(a)].

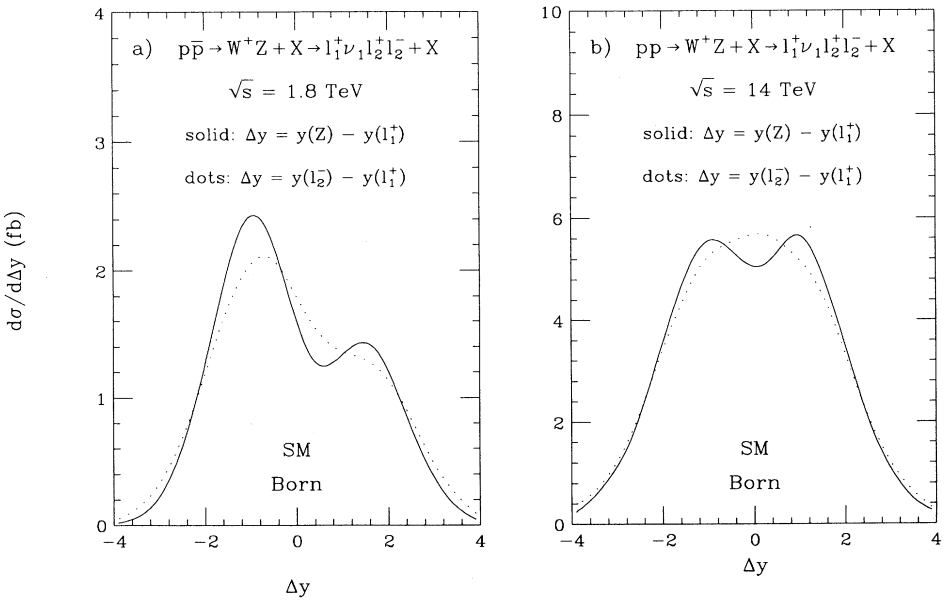

FIG. 17. SM rapidity difference distributions in the Born approximation for (a) $p\bar{p} \to W^+Z + X \to \ell_1^+\nu_1\ell_2^+\ell_2^- + X$ at $\sqrt{s} = 1.8$ TeV and (b) $pp \to W^+Z + X \to \ell_1^+\nu_1\ell_2^+\ell_2^- + X$ at $\sqrt{s} = 14$ TeV. The curves are for $y(Z) - y(\ell_1^+)$ (solid lines) and $y(\ell_2^-) - y(\ell_1^+)$ (dotted lines). The cuts imposed are summarized in Sec. III B.

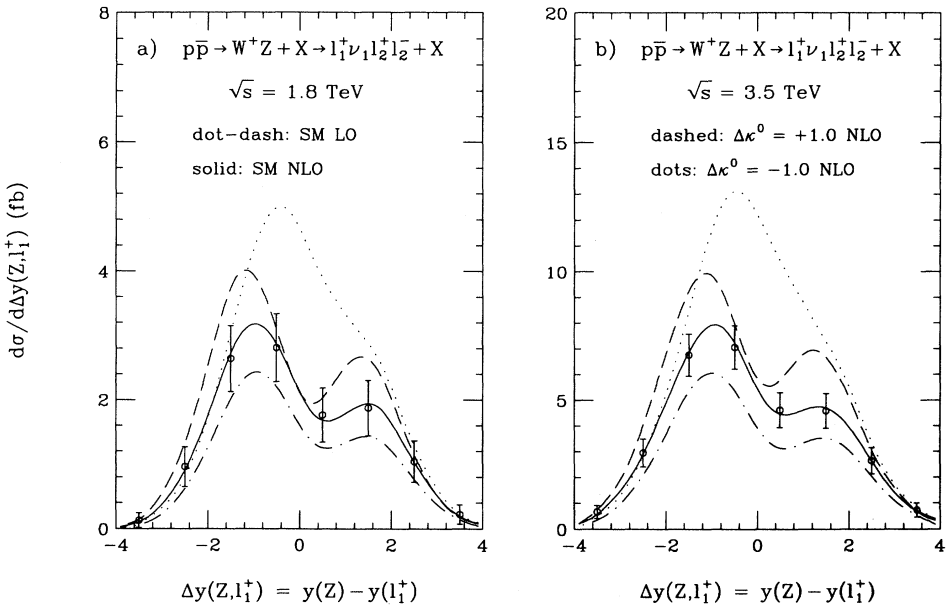

FIG. 18. The differential cross section for the rapidity difference $\Delta y(Z, \ell_1)$ for $p\bar{p} \to W^+Z + X \to \ell_1^+\nu_1\ell_2^+\ell_2^- + X$ (a) at $\sqrt{s} = 1.8$ TeV and (b) at $\sqrt{s} = 3.5$ TeV. The solid and dot-dashed curves show the inclusive NLO and the LO SM predictions, respectively. The dashed and dotted lines give the results for $\Delta\kappa^0 = +1$ and $\Delta\kappa^0 = -1$, respectively. The error bars associated with the solid curves indicate the expected statistical uncertainties for an integrated luminosity of 10 fb^{-1}. The cuts imposed are summarized in Sec. III B.

The effect of anomalous WWZ couplings on the NLO $\Delta y(Z, \ell_1)$ distribution is exemplified by the dashed and dotted lines in Fig. 18 and in Fig. 19(b). Similar to the situation encountered in the $|y^*(Z)|$ distribution, the dip in the $\Delta y(Z, \ell_1)$ distribution at Tevatron and DiTevatron energies may be more pronounced than in the SM for certain (positive) values of $\Delta\kappa^0$. The shape of the $\Delta y(Z, \ell_1)$ distribution is seen to be quite sensitive to the sign of $\Delta\kappa^0$ (Fig. 18). The same behavior is observed for Δg_1^0, whereas positive and negative values of λ^0 lead to a very similar $\Delta y(Z, \ell_1)$ distribution. In general, nonstandard WWZ couplings tend to fill in the dip. In order not

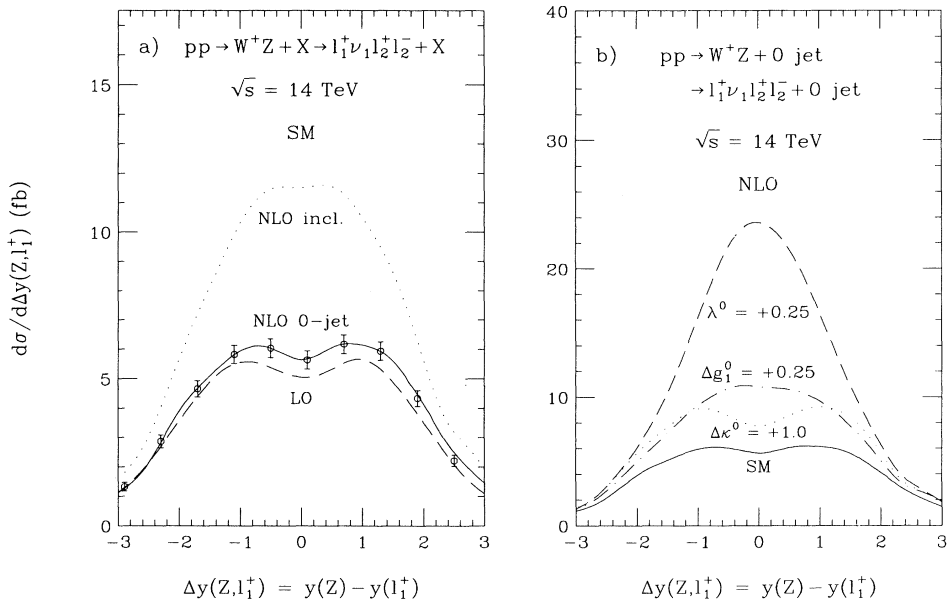

FIG. 19. The differential cross section for the rapidity difference $\Delta y(Z, \ell_1)$ at $\sqrt{s} = 14$ TeV for (a) $pp \to W^+Z + X \to \ell_1^+\nu_1\ell_2^+\ell_2^- + X$ in the SM and (b) for $pp \to W^+Z + 0$ jet $\to \ell_1^+\nu_1\ell_2^+\ell_2^- + 0$ jet at NLO. In part (a) the dotted and dashed curves show the inclusive NLO and the LO SM predictions, respectively, while the solid curve gives the prediction for the SM NLO $WZ + 0$ jet case. The error bars associated with the solid curve indicate the expected statistical uncertainties for an integrated luminosity of 100 fb^{-1}. In part (b) the curves are for the SM (solid line), $\Delta\kappa^0 = +1$ (dotted line), $\lambda^0 = +0.25$ (dashed curve), and $\Delta g_1^0 = +0.25$ (dot-dashed curve). The cuts imposed are summarized in Sec. III B. For the jet definition, we have used Eq. (14).

to overburden the figures, curves for λ^0 and Δg_1^0 are not shown in Fig. 18. If deviations from the SM prediction were to be observed, it would be difficult to determine the sign of an anomalous coupling from the shape of the WZ invariant mass distribution, the cluster transverse mass spectrum, or the $p_T(Z)$ distribution. For $\Delta\kappa^0$ and Δg_1^0, the pronounced difference in shape of the $\Delta y(Z,\ell_1)$ distribution for positive and negative values may aid in determining the sign. The influence of nonstandard WWZ couplings on the exclusive NLO $WZ+0$ jet distribution is shown in Fig. 19(b). Curves are only shown for positive values of the anomalous couplings.

The error bars associated with the solid curves in Figs. 18 and 19(a) indicate the expected statistical uncertainties for an integrated luminosity of 10 fb^{-1} at the Tevatron and DiTevatron, and for $\int \mathcal{L}dt = 100$ fb^{-1} at the LHC. It appears that the approximate zero in the WZ amplitude will be rather difficult to observe in the $\Delta y(Z,\ell_1)$ distribution. However, if the LHC is operated below its design luminosity of $\mathcal{L} = 10^{34}$ cm^{-2} s^{-1}, it may be possible to reduce the $\not{p}_T$ cut. As mentioned above, the significance of the dip in the $\Delta y(Z,\ell_1)$ distribution increases if the missing transverse momentum cut is lowered. The smaller collision rate is at least partially compensated by the larger total cross section for the reduced $\not{p}_T$ cut. It is thus possible that the conditions to detect the dip in the $\Delta y(Z,\ell_1)$ distribution improve if the LHC is operated below its design luminosity. However, more detailed simulations are required before definite conclusions can be drawn.

As an alternative to rapidity correlations, cross section ratios can be studied. Many experimental uncertainties, for example, those associated with the lepton detection efficiencies or the uncertainty in the integrated luminosity, are expected to cancel, at least partially, in the cross section ratios. In Ref. [14], the ratio of the $Z\gamma$ to $W\gamma$ cross sections, $\mathcal{R}_{Z\gamma/W\gamma}$, was shown to reflect the radiation zero present in the SM $W\gamma$ helicity amplitudes. Because of the radiation zero, the $W\gamma$ cross section is reduced in the central rapidity region. With increasing photon transverse momenta, events become more and more central in rapidity. The reduction of the $W\gamma$ cross section at small rapidities originating from the radiation zero thus becomes more pronounced at high $p_T(\gamma)$. This causes the photon transverse momentum distribution of $q_1\bar{q}_2 \to W\gamma$ to fall significantly faster than the $p_T(\gamma)$ spectrum of $q\bar{q} \to Z\gamma$ where no radiation zero is present. As a result, $\mathcal{R}_{Z\gamma/W\gamma}$ increases rapidly with the minimum transverse momentum of the photon.

In Fig. 20 we study the cross section ratio

$$\mathcal{R}_{ZZ/WZ} = \frac{B^2(Z\to\ell^+\ell^-)\,\sigma(ZZ)}{B(Z\to\ell^+\ell^-)\,B(W\to\ell\nu)\,\sigma(W^\pm Z)} = \frac{B(Z\to\ell^+\ell^-)\,\sigma(ZZ)}{B(W\to\ell\nu)\,\sigma(W^\pm Z)}\,, \tag{18}$$

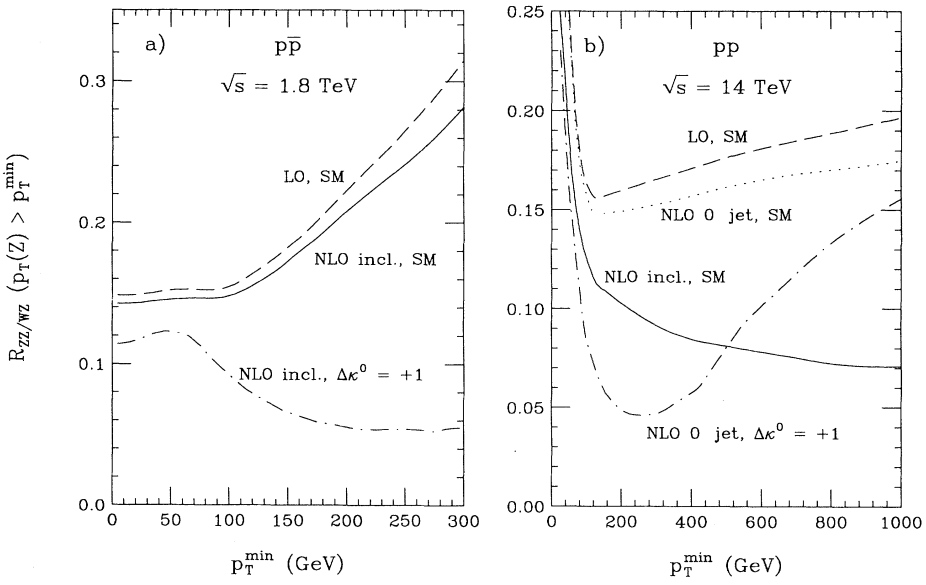

FIG. 20. The ratio $\mathcal{R}_{ZZ/WZ} = B(Z\to\ell^+\ell^-)\,\sigma(ZZ)/B(W\to\ell\nu)\,\sigma(W^\pm Z)$, $\ell = e,\ \mu$, as a function of the minimum transverse momentum of the Z boson, $p_T^{\min}$, at (a) the Tevatron and (b) the LHC. The solid and dashed lines show the inclusive NLO and the LO results for the SM, respectively. The dotted line in (b) gives the SM cross section ratio at NLO if a 0-jet requirement is imposed. The dot-dashed line displays $\mathcal{R}_{ZZ/WZ}$ for $\Delta\kappa^0 = +1$. In part (a) this curve is calculated taking into account inclusive $O(\alpha_s)$ QCD corrections, whereas in part (b) the dot-dashed curve is for the NLO 0-jet cross section ratio. The cuts imposed are summarized in Sec. III B. For the jet definition, we have used Eq. (14).

as a function of the minimum transverse momentum of the Z boson, $p_T^{\min}$. To calculate the ZZ cross section, we use the results of Ref. [15] and assume the SM to be valid. The ZZ helicity amplitudes do not exhibit any zeros, whereas the SM WZ amplitude shows an approximate zero in the central rapidity region. The situation is thus qualitatively very similar to that encountered in the ratio of $Z\gamma$ to $W\gamma$ cross sections, and one expects $\mathcal{R}_{ZZ/WZ}$ to grow with $p_T^{\min}$. Figure 20(a) demonstrates that, at Tevatron energies, $\mathcal{R}_{ZZ/WZ}$ indeed rises quickly for $p_T^{\min} > 100$ GeV in the SM, indicating the presence of the approximate zero in the WZ amplitude. For smaller values of the minimum Z boson transverse momentum, $\mathcal{R}_{ZZ/WZ}$ is approximately constant. In the low $p_T^{\min}$ region, the shape of the $p_T(Z)$ distribution is dominated by Z mass effects which are similar in both processes. The cross section ratio at next-to-leading-order differs only by about 10% from the LO ratio.

At LHC energies, the situation is more complex. For $p_T^{\min} < 100$ GeV, $\mathcal{R}_{ZZ/WZ}$ drops sharply due to the large $\not{p}_T$ cut imposed, which significantly suppresses the WZ cross section. While the cross section ratio slowly rises with $p_T^{\min}$ for $p_T^{\min} > 100$ GeV at leading-order, $\mathcal{R}_{ZZ/WZ}$ continues to decrease if inclusive $O(\alpha_s)$ QCD corrections are taken into account [Fig. 20(b)]. The relatively slower rise of $\mathcal{R}_{ZZ/WZ}$ at LO at the LHC is due to the larger fraction of the cross sections originating from sea quark collisions, and the different x ranges probed at the Tevatron and LHC. For $p_T^{\min}(Z) = 1$ TeV, the inclusive NLO cross section ratio is about a factor 3 smaller than $\mathcal{R}_{ZZ/WZ}$ at leading-order. At large values of the Z boson transverse momentum, the QCD corrections to WZ production at LHC energies are substantially larger than in the ZZ case [15], resulting in a large discrepancy between the LO and NLO prediction for $\mathcal{R}_{ZZ/WZ}$. In contrast with the situation encountered at the Tevatron, higher order QCD corrections completely blur the signal of the approximate amplitude zero in the WZ channel. Their size, however, can be substantially reduced by imposing a zero jet requirement (see Sec. III E and Ref. [15]). The result for the $ZZ + 0$ jet to $W^{\pm}Z + 0$ jet cross section ratio at the LHC is given by the dotted line in Fig. 20(b). With a jet veto imposed, the NLO ZZ-to-WZ cross section ratio rises with the minimum Z boson transverse momentum for $p_T^{\min} > 100$ GeV, and differs by at most 15% from the LO prediction. At the Tevatron, the NLO 0-jet cross section ratio virtually coincides with the ratio obtained at LO.

The dot-dashed curve in Fig. 20, finally, shows the ZZ-to-WZ cross section ratio for $\Delta\kappa^0 = +1$, illustrating the behavior of $\mathcal{R}_{ZZ/WZ}$ in the presence of anomalous WWZ couplings. At the Tevatron [Fig. 20(a)], the dot-dashed curve has been calculated taking into account inclusive $O(\alpha_s)$ QCD corrections. At LHC energies [Fig. 20(b)], the NLO ZZ-to-WZ cross section ratio is plotted with a jet veto included. Nonstandard couplings lead to an enhancement of the WZ cross section, in particular at large values of $p_T(Z)$ and, at the Tevatron, $\mathcal{R}_{ZZ/WZ}$ decreases with $p_T^{\min}$. Because of the form factor parameters assumed ($n = 2$ and $\Lambda_{\rm FF} = 1$ TeV), the cross section ratio at the LHC displays a broad minimum at $p_T^{\min}(Z) \approx 300$ GeV, and increases quickly at large values of $p_T^{\min}$. For larger values of $\Lambda_{\rm FF}$ and/or nonzero values of Δg_1^0 or λ^0, $\mathcal{R}_{ZZ/WZ}$ rises more slowly, or may even decrease with $p_T^{\min}(Z)$. In general, the ZZ-to-WZ cross section ratio as a function of the minimum Z boson transverse momentum differs substantially in shape from the SM prediction for $\mathcal{R}_{ZZ/WZ}$ in the presence of nonstandard WWZ couplings.

At the Tevatron, the limited number of ZZ and WZ events expected in the purely leptonic channels will unfortunately limit the usefulness of $\mathcal{R}_{ZZ/WZ}$. Even for an integrated luminosity of 10 fb^{-1} only a handful of events are expected for $p_T(Z) > 150$ GeV, and it will be very difficult to establish the growth with $p_T^{\min}(Z)$ predicted by the SM. At the LHC, the statistical errors are expected to be much smaller; however, one can only hope to observe the rise of $\mathcal{R}_{ZZ/WZ}$ signaling the presence of the approximate zero in the WZ channel if a 0-jet requirement is imposed. Moreover, the rise of the cross section ratio is very slow, and for $p_T^{\min} = 600$ GeV only about five (two) purely leptonic $W^{\pm}Z$ (ZZ) events are expected for $\int \mathcal{L} dt = 100$ fb^{-1}. Combined, these effects will make it quite difficult to accurately determine the slope of $\mathcal{R}_{ZZ/WZ}$.

A cross section ratio which suffers somewhat less from the small number of events expected at the Tevatron and which is less sensitive to QCD corrections at the LHC is the ratio of WZ to $W\gamma$ cross sections,

$$\mathcal{R}_{WZ/W\gamma} = \frac{B(Z \to \ell^+\ell^-)\, B(W \to \ell\nu)\, \sigma(W^{\pm}Z)}{B(W \to \ell\nu)\, \sigma(W^{\pm}\gamma)} = B(Z \to \ell^+\ell^-)\, \frac{\sigma(W^{\pm}Z)}{\sigma(W^{\pm}\gamma)}, \tag{19}$$

considered as a function of the minimum transverse momentum of the Z boson and photon, $p_T^{\min}$, respectively. $\mathcal{R}_{WZ/W\gamma}$ measures the relative strength of the approximate zero in $q_1\bar{q}_2 \to WZ$ and the radiation zero in $W\gamma$ production. Figure 21 shows the ratio $\mathcal{R}_{WZ/W\gamma}$ as a function of $p_T^{\min}$ for the Tevatron [part (a)] and LHC [part (b)] center-of-mass energies. In obtaining $\mathcal{R}_{WZ/W\gamma}$, we have considered both the electron and muon decay channels of the W and Z bosons. The $W\gamma$ cross section in Fig. 21 has been calculated using the results of Ref. [49] and the following cuts on the photon:

$$\begin{aligned} p_T(\gamma) &> 10 \text{ GeV}, & |\eta(\gamma)| &< 1, \quad \text{(Tevatron)} \\ p_T(\gamma) &> 100 \text{ GeV}, & |\eta(\gamma)| &< 2.5, \quad \text{(LHC)} \\ M_T(\ell\gamma; \not{p}_T) &> 90 \text{ GeV}, & \Delta R(\gamma, \ell) &> 0.7. \end{aligned} \tag{20}$$

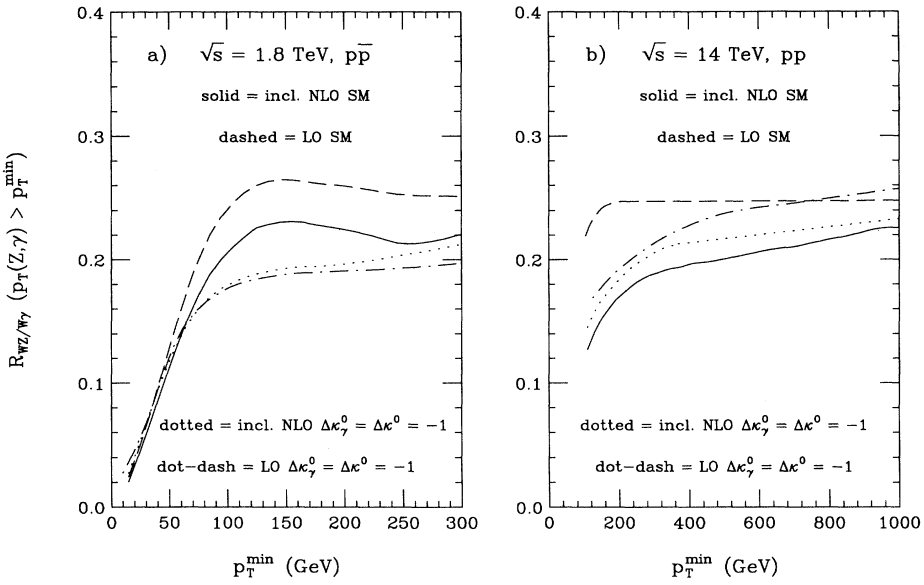

FIG. 21. The ratio $\mathcal{R}_{WZ/W\gamma} = B(Z \to \ell^+\ell^-)\sigma(W^\pm Z)/\sigma(W^\pm\gamma)$, $\ell = e, \mu$, as a function of the minimum transverse momentum of the Z boson and photon, $p_T^{\min}$, respectively, at (a) the Tevatron and (b) the LHC. The solid and dashed lines show the inclusive NLO and the LO results for the SM, respectively. The dotted and dot-dashed lines display the inclusive NLO and LO WZ-to-$W\gamma$ cross section ratio for $\Delta\kappa_\gamma^0 = \Delta\kappa^0 = -1$. Here, $\Delta\kappa_\gamma$ is the anomalous $WW\gamma$ coupling defined in an analogous way to $\Delta\kappa$ [see Eq. (1)]. The cuts imposed are summarized in Sec. III B and Eq. (20).

At small values of $p_T^{\min}$, the WZ-to-$W\gamma$ cross section ratio rises very rapidly, due to the finite Z mass effects which dominate the shape of the $p_T(Z)$ spectrum in this region for WZ production. For $p_T^{\min} > 100$ GeV (200 GeV) at the Tevatron (LHC), $\mathcal{R}_{WZ/W\gamma}$ is almost constant and independent of the center-of-mass energy, indicating that the radiation zero in $q_1\bar{q}_2 \to W\gamma$ and the approximate amplitude zero in WZ production affect the respective photon and Z boson transverse momentum distribution in a very similar way. At the Tevatron, $O(\alpha_s)$ QCD corrections reduce $\mathcal{R}_{WZ/W\gamma}$ by about 10%. At LHC energies, the individual $O(\alpha_s)$ QCD corrections are very large for both WZ and $W\gamma$ production [49], in particular at high transverse momenta (see Figs. 9 and 12). In the cross section ratio, these large corrections cancel almost completely. For $p_T^{\min} > 200$ GeV, QCD corrections reduce $\mathcal{R}_{WZ/W\gamma}$ by 20% or less. In contrast to the LO cross section ratio, which is completely flat for $p_T^{\min} > 200$ GeV, $\mathcal{R}_{WZ/W\gamma}$ at NLO slowly rises with $p_T^{\min}$ at the LHC.

Most theoretical models with nonstandard WWZ couplings also predict anomalous $WW\gamma$ couplings at the same time (see, e.g., Ref. [21]). The effects of anomalous WWZ and $WW\gamma$ couplings may cancel almost completely in $\mathcal{R}_{WZ/W\gamma}$ if the WWZ and $WW\gamma$ couplings are similar in magnitude and originate from operators of the same dimension. This is illustrated by the dot-dashed and dotted lines in Fig. 21, which show $\mathcal{R}_{WZ/W\gamma}$ at LO and NLO for $\Delta\kappa_\gamma^0 = \Delta\kappa^0 = -1$. Here the anomalous $WW\gamma$ coupling $\Delta\kappa_\gamma$ is defined through an effective Lagrangian analogous to that of Eq. (1), and we assume equal form factor scales and powers ($\Lambda_{\rm FF} = 1$ TeV and $n = 2$) for $\Delta\kappa$ and $\Delta\kappa_\gamma$. Both couplings correspond to operators of dimension 4 in the effective Lagrangian. Although the individual $p_T(\gamma)$ and $p_T(Z)$ differential cross sections are enhanced by up to one order of magnitude (see, e.g., Figs. 7 and 9), $\mathcal{R}_{WZ/W\gamma}$ agrees to better than 20% with the NLO SM cross section ratio for $\Delta\kappa_\gamma^0 = \Delta\kappa^0 = -1$.

At DiTevatron energies, the results for $\mathcal{R}_{ZZ/WZ}$ and $\mathcal{R}_{WZ/W\gamma}$ are qualitatively similar to those obtained for Tevatron and are therefore not shown.

V. SUMMARY

WZ production in hadronic collisions provides an opportunity to probe the structure of the WWZ vertex in a direct and essentially model independent way. Previous studies of $p\overset{(-)}{p} \to W^\pm Z$ [3,4] have been based on leading-order calculations. In this paper we have presented an $O(\alpha_s)$ calculation of the reaction $p\overset{(-)}{p} \to W^\pm Z + X \to \ell_1^\pm\nu_1\ell_2^+\ell_2^- + X$ for general, C- and P-conserving WWZ couplings, using a combination of analytic and Monte Carlo integration techniques. The leptonic decays $W \to \ell_1\nu_1$ and $Z \to \ell_2^+\ell_2^-$ have been included in the narrow width approximation in our calculation. Decay spin correlations are correctly taken into account in our approach, except in the finite virtual contribution. The finite virtual correction term contributes only at the few percent level to the total NLO cross section; thus decay spin correlations can be safely ignored here.

The $p_T(Z)$ differential cross section is very sensitive to nonstandard WWZ couplings. We found that QCD corrections significantly change the shape of this distribution at very high energies [see Fig. 9 and 10(b)]. This shape change is due to a combination of destructive interference in the WZ Born subprocess and a logarithmic enhancement factor in the qg and $\bar{q}g$ real emission subprocesses. The destructive interference suppresses the size of the

WZ Born cross section and is also responsible for the approximate amplitude zero in $q_1\bar{q}_2 \to WZ$ [5]. The logarithmic enhancement factor originates in the high $p_T(Z)$ $[p_T(W)]$ region of phase space where the Z $[W]$ boson is balanced by a high p_T quark which radiates a soft W $[Z]$ boson. The logarithmic enhancement factor and the large gluon density at high center-of-mass energies make the $O(\alpha_s)$ corrections large for $p_T(Z) \gg M_Z$. Since the Feynman diagrams responsible for the enhancement at large $p_T(Z)$ do not involve the WWZ vertex, inclusive $O(\alpha_s)$ QCD corrections to $W^{\pm}Z$ production tend to reduce the sensitivity to nonstandard couplings. QCD corrections in WZ production thus exhibit the same features which characterize the $O(\alpha_s)$ corrections in $W\gamma$ production.

At the Tevatron and DiTevatron, WZ production proceeds mainly via quark-antiquark annihilation and, for the expected integrated luminosities (≤ 10 fb^{-1}), large transverse momenta are not accessible. As a result, the sensitivity reduction in the high p_T tail caused by the QCD corrections is balanced by the larger cross section at $O(\alpha_s)$, and the limits derived from the NLO and LO $p_T(Z)$ distributions are very similar (see Table I). At the LHC, however, where the qg luminosity is very high and the change in slope of the SM $p_T(Z)$ distribution from QCD corrections is very pronounced, the sensitivity bounds which can be achieved are weakened by up to 40% (see Table II).

The size of the QCD corrections at large $p_T(Z)$ may be reduced substantially, and a fraction of the sensitivity to anomalous WWZ couplings which was lost at the LHC may be regained, by imposing a jet veto, i.e., by considering the exclusive $WZ + 0$ jet channel instead of inclusive $WZ + X$ production. The improvement is equivalent to roughly a factor of 1.5–2.5 increase in integrated luminosity. The dependence of the NLO $WZ + 0$ jet cross section on the factorization scale Q^2 is significantly reduced compared to that of the inclusive NLO $WZ + X$ cross section. Uncertainties which originate from the variation of Q^2 will thus be smaller for sensitivity bounds obtained from the $WZ + 0$ jet channel than for those derived from the inclusive NLO $WZ + X$ cross section. At the Tevatron (DiTevatron), $O(\alpha_s)$ QCD corrections do not influence the sensitivity limits in a significant way. Nevertheless, it will be important to take these corrections into account when extracting information on the structure of the WWZ vertex, in order to reduce systematic and theoretical errors.

At the Tevatron (DiTevatron) with $\int \mathcal{L} dt = 10$ fb^{-1}, taking into account all correlations between the different WWZ couplings, $\Delta\kappa^0$ can be measured with 70–100% (50–60%) accuracy in WZ production in the purely leptonic channels, whereas the two other couplings can be determined with an uncertainty of 0.1–0.25. At the LHC with $\int \mathcal{L} dt = 100$ fb^{-1}, $\Delta\kappa^0$ can be determined with an uncertainty of about 10%, whereas Δg_1^0 and λ^0 can be measured to better than 0.01, with details depending on the form factor scale assumed (see Table II).

The bounds listed in Tables I and II should be compared with the limits which can be obtained in other channels and at e^+e^- colliders. Assuming SM $WW\gamma$ couplings, Δg_1^0 and λ^0 can be measured in $p\bar{p} \to W^+W^-, W^{\pm}Z \to \ell^{\pm}\nu jj$ with a precision similar to that which can be achieved in the $W^{\pm}Z \to \ell_1^{\pm}\nu_1\ell_2^+\ell_2^-$ mode, both at the Tevatron with 1 fb^{-1} and the TeV*. The limits which can be obtained for $\Delta\kappa^0$ from the $\ell^{\pm}\nu jj$ final state are about a factor of 4 better than those from double leptonic WZ decays [53]. The bounds which can be achieved for $\Delta\kappa^0$, Δg_1^0, and λ^0 in $e^+e^- \to W^+W^-$ at LEP II depend quite sensitively on the center-of-mass energy. For $\sqrt{s} = 176$ GeV and $\int \mathcal{L} dt = 500$ pb^{-1}, the WWZ couplings can be measured with a precision of about ± 0.5, if correlations between the three couplings are taken into account [53,58]. At a linear e^+e^- collider with a center-of-mass energy of 500 GeV or higher, they can be determined with an accuracy of better than 0.01 [53,59].

We also studied possible experimental signals of the approximate zero in the SM WZ amplitude. Unlike the situation encountered in $W\gamma$ production where the radiation zero leads to a pronounced minimum in the photon-lepton rapidity difference distribution, the approximate amplitude zero in WZ production causes a slight dip only in the corresponding $\Delta y(Z, \ell_1) = y(Z) - y(\ell_1)$ distribution. In $W^{\pm}\gamma$ production, the dominant W helicity is $\lambda_W = \pm 1$, implying that the charged lepton from the decaying W boson tends to be emitted in the direction of the parent W boson, and thus reflects most of its kinematic properties. In contrast, none of the W helicities dominates in WZ production. The charged lepton originating from the W boson decay $W \to \ell_1\nu_1$ thus only partly reflects the kinematic properties of the parent W boson, which reduces the significance of the dip. At Tevatron and DiTevatron energies, higher order QCD corrections only negligibly influence the shape of the $\Delta y(Z, \ell_1)$ distribution. At the LHC, however, $O(\alpha_s)$ QCD effects completely obscure the dip, unless a 0-jet requirement is imposed.

Alternatively, cross section ratios can be used to search for experimental indications of the approximate amplitude zero. We found that the ratio of ZZ to WZ cross sections as a function of the minimum Z boson transverse momentum $p_T^{\min}$ increases with $p_T^{\min}$ for values larger than 100 GeV. The increase of the ratio of ZZ to WZ cross sections is a direct consequence of the approximate zero. The ratio of WZ to $W\gamma$ cross sections, on the other hand, is almost independent of the minimum p_T of the Z boson and photon for sufficiently large values of $p_T^{\min}$, indicating that the approximate zero in WZ production and the radiation zero in $W\gamma$ production affect the Z boson and photon transverse momentum distributions in a very similar way. QCD corrections have a significant impact on the ZZ-to-WZ cross section ratio at the LHC unless a jet veto is imposed, whereas they largely cancel in the WZ-to-$W\gamma$ cross section ratio.

Together with the $\Delta y(Z, \ell_1)$ distribution, the ZZ-to-$W^{\pm}Z$ and WZ-to-$W\gamma$ cross section ratios are useful tools in searching for the approximate amplitude zero in WZ production. However, for the integrated luminosities envisioned, it will not be easy to conclusively establish the approximate amplitude zero in WZ production at the Tevatron or the LHC.

ACKNOWLEDGMENTS

We would like to thank B. Choudhury, T. Fuess, C. Wendt, and D. Zeppenfeld for stimulating discussions. Two of us (U.B. and T.H.) wish to thank the Fermilab Theory Group for its warm hospitality during various stages of this work. This work has been supported in part by Department of Energy Grants Nos. DE-FG03-91ER40674 and DE-FG05-87ER40319 and by Texas National Research Laboratory Grant No. RGFY93-330. T.H. was also supported in part by a UC-Davis Faculty research grant.

[1] R. W. Brown, K. O. Mikaelian, and D. Sahdev, Phys. Rev. D **20**, 1164 (1979).

[2] E. Eichten, I. Hinchliffe, K. Lane, and C. Quigg, Rev. Mod. Phys. **56**, 579 (1984); **58**, 1065(E) (1986).

[3] D. Zeppenfeld and S. Willenbrock, Phys. Rev. D **37**, 1775 (1988).

[4] M. Kuroda, J. Maalampi, K. H. Schwarzer, and D. Schildknecht, Nucl. Phys. **B284**, 271 (1987); S.-C. Lee and W.-C. Su, Phys. Lett. B **212**, 113 (1988); K. Hagiwara, J. Woodside, and D. Zeppenfeld, Phys. Rev. D **41**, 2113 (1990); H. Kuijf *et al.*, in *Proceedings of the ECFA Large Hadron Collider Workshop*, Aachen, Germany, 1990, edited by G. Jarlskog and D. Rein (CERN Report No. 90-10, Geneva, Switzerland, 1990), Vol. II, p. 91.

[5] U. Baur, T. Han, and J. Ohnemus, Phys. Rev. Lett. **72**, 3941 (1994).

[6] K. O. Mikaelian, Phys. Rev. D **17**, 750 (1978); K. O. Mikaelian, M. A. Samuel, and D. Sahdev, Phys. Rev. Lett. **43**, 746 (1979); D. Zhu, Phys. Rev. D **22**, 2266 (1980); T. R. Grose and K. O. Mikaelian, *ibid.* **23**, 123 (1981); C. J. Goebel, F. Halzen, and J. P. Leveille, *ibid.* **23**, 2682 (1981); S. J. Brodsky and R. W. Brown, Phys. Rev. Lett. **49**, 966 (1982); M. A. Samuel, Phys. Rev. D **27**, 2724 (1983); R. W. Brown, K. L. Kowalski, and S. J. Brodsky, *ibid.* **28**, 624 (1983); R. W. Brown and K. L. Kowalski, *ibid.* **29**, 2100 (1984).

[7] CDF Collaboration, F. Abe *et al.*, presented at the 27th International Conference on High Energy Physics, Glasgow, Scotland, 1994 (unpublished).

[8] D. Amidei *et al.*, in *Proceedings of the DPF'94 Conference*, Albuquerque, New Mexico, 1994 (in press); S. Holmes, G. Dugan, and S. Peggs, in *Research Directions for the Decade, Proceedings of the 1990 Summer Study on High Energy Physics,* Snowmass, Colorado, edited by E. L. Berger (World Scientific, Singapore, 1991), p. 674.

[9] The LHC Study Group, "Design Study of the Large Hadron Collider," Report No. CERN 91-03, 1991 (unpublished).

[10] J. Ohnemus, Phys. Rev. D **44**, 3477 (1991).

[11] S. Frixione, P. Nason, and G. Ridolfi, Nucl. Phys. **B383**, 3 (1992).

[12] H. Baer, J. Ohnemus, and J. F. Owens, Phys. Rev. D **40**, 2844 (1989); **42**, 61 (1990); Phys. Lett. B **234**, 127 (1990); J. Ohnemus and J. F. Owens, Phys. Rev. D **43**, 3626 (1991); J. Ohnemus, *ibid.* **44**, 1403 (1991); **44**, 3477 (1991); H. Baer and M. H. Reno, *ibid.* **43**, 2892 (1991); B. Bailey, J. Ohnemus, and J. F. Owens, *ibid.* **46**, 2018 (1992); J. Ohnemus, *ibid.* **47**, 940 (1993); J. Ohnemus and W. J. Stirling, *ibid.* **47**, 2722 (1993); H. Baer, B. Bailey, and J. F. Owens, *ibid.* **47**, 2730 (1993); L. Bergmann, Ph.D. dissertation, Florida State University, 1989.

[13] U. Baur, S. Errede, and G. Landsberg, Phys. Rev. D **50**, 1917 (1994).

[14] U. Baur, S. Errede, and J. Ohnemus, Phys. Rev. D **48**, 4103 (1993).

[15] J. Ohnemus, Phys. Rev. D **50**, 1931 (1994).

[16] U. Baur, E. W. N. Glover, and J. J. van der Bij, Nucl. Phys. **B318**, 106 (1989); V. Barger, T. Han, J. Ohnemus, and D. Zeppenfeld, Phys. Rev. D **41**, 2782 (1990).

[17] K. Hagiwara, R. D. Peccei, D. Zeppenfeld, and K. Hikasa, Nucl. Phys. **B282**, 253 (1987); K. Gaemers and G. Gounaris, Z. Phys. C **1**, 259 (1979).

[18] CDF Collaboration, T. A. Fuess, *Proceedings of the DPF'94 Conference* [8].

[19] A. De Rujula *et al.*, Nucl. Phys. **B384**, 31 (1992); P. Hernández and F. J. Vegas, Phys. Lett. B **307**, 116 (1993).

[20] C. Burgess and D. London, Phys. Rev. Lett. **69**, 3428 (1992); Phys. Rev. D **48**, 4337 (1993).

[21] K. Hagiwara, S. Ishihara, R. Szalapski, and D. Zeppenfeld, Phys. Lett. B **283**, 353 (1992); Phys. Rev. D **48**, 2182 (1993).

[22] X. He, Phys. Lett. B **319**, 327 (1993).

[23] G. Baillie, Z. Phys. C **61**, 667 (1994).

[24] X. He and B. McKellar, Report No. OITS-541A, 1994 (unpublished).

[25] G. Belanger, F. Boudjema, and D. London, Phys. Rev. Lett. **65**, 2943 (1990); O. Eboli *et al.*, Phys. Lett. B **339**, 119 (1994).

[26] A. Falk, M. Luke, and E. Simmons, Nucl. Phys. **B365**, 523 (1991).

[27] J. Bagger, S. Dawson, and G. Valencia, Nucl. Phys. **B399**, 364 (1993); M. J. Herrero and E. Ruiz Morales, *ibid.* **B418**, 431 (1994); C. Arzt, M. B. Einhorn, and J. Wudka, Report No. UM-TH-94-15, 1994 (unpublished); J. Wudka, Int. J. Mod. Phys. A **9**, 2301 (1994).

[28] J. A. M. Vermaseren, *FORM User's Manual* (NIKHEF-H, Amsterdam, 1989).

[29] J. M. Cornwall, D. N. Levin, and G. Tiktopoulos, Phys. Rev. Lett. **30**, 1268 (1973); Phys. Rev. D **10**, 1145 (1974); C. H. Llewellyn Smith, Phys. Lett. **46B**, 233 (1973); S. D. Joglekar, Ann. Phys. (N.Y.) **83**, 427 (1974).

[30] U. Baur and D. Zeppenfeld, Phys. Lett. B **201**, 383 (1988).

[31] U. Baur and D. Zeppenfeld, Nucl. Phys. **B308**, 127 (1988).

[32] D0 Collaboration, S. Abachi *et al.*, Phys. Rev. Lett. **72**, 2138 (1994).

[33] CDF Collaboration, F. Abe *et al.*, Phys. Rev. Lett. **73**, 225 (1994); Phys. Rev. D **50**, 2966 (1994).

[34] LEP Collaborations, D. Decamp *et al.*, Phys. Lett. B **276**, 247 (1992); Report No. CERN/PPE/93-157, 1993 (unpublished); B. Pietrzyk, in the *Proceedings of the XXIXth Recontres de Moriond*, Méribel, France, 1994 (in press).

[35] SLD Collaboration, K. Abe *et al.*, Phys. Rev. Lett. **73**, 25 (1994).

[36] D. Schaile, Z. Phys. C **54**, 387 (1992).

[37] UA2 Collaboration, J. Alitti *et al.*, Phys. Lett. B **241**, 150 (1990); CDF Collaboration, F. Abe *et al.*, Phys. Rev. Lett. **65**, 2243 (1990); Phys. Rev. D **43**, 2070 (1991); K. Hara, talk given at the INS Symposium, Tokyo, Japan, 1994, Report No. FERMILAB-Conf-94/088-E (unpublished).
[38] A. D. Martin, R. G. Roberts, and W. J. Stirling, Phys. Lett. B **306**, 145 (1993).
[39] NMC, P. Amaudruz *et al.*, Phys. Lett. B **295**, 159 (1992).
[40] CCFR Collaboration, S. R. Mishra *et al.*, Report No. NEVIS-1459, 1992 (unpublished)
[41] H1 Collaboration, T. Ahmed *et al.*, Phys. Lett. B **299**, 385 (1993); H1 Collaboration, I. Abt *et al.*, Nucl. Phys. **B407**, 515 (1993); Phys. Lett. B **321**, 161 (1994); ZEUS Collaboration, M. Derrick *et al.*, Phys. Lett. B **303**, 183 (1993); **316**, 412 (1993); Report No. DESY 94-143, 1994 (unpublished).
[42] C. Albajar *et al.*, in *Proceedings of the ECFA Large Hadron Collider Workshop* [4], Vol. II, p. 621.
[43] ATLAS Collaboration, D. Gingrich *et al.*, Report No. CERN-LHCC-92-4, 1992 (unpublished).
[44] CMS Collaboration, M. Della Negra *et al.*, Report No. CERN-LHCC-92-3, 1992 (unpublished).
[45] CDF Collaboration, F. Abe *et al.*, Phys. Rev. D **45**, 3921 (1992).
[46] J. Stroughair and C. Bilchak, Z. Phys. C **26**, 415 (1984); J. Gunion, Z. Kunszt, and M. Soldate, Phys. Lett. **163B**, 389 (1985); J. Gunion and M. Soldate, Phys. Rev. D **34**, 826 (1986); W. J. Stirling *et al.*, Phys. Lett. **163B**, 261 (1985).
[47] J. Cortes, K. Hagiwara, and F. Herzog, Nucl. Phys. **B278**, 26 (1986).
[48] V. Barger, A. D. Martin, and R. J. N. Phillips, Phys. Lett. **125B**, 339 (1983); E. L. Berger, D. DiBitonto, M. Jacob, and W. J. Stirling, *ibid.* **140B**, 259 (1984).
[49] U. Baur, T. Han, and J. Ohnemus, Phys. Rev. D **48**, 5140 (1993).
[50] T. Han, R. Meng, and J. Ohnemus, Nucl. Phys. **B384**, 59 (1992); P. Arnold and R. Kauffman, *ibid.* **B349**, 381 (1991); R. Kauffman, Phys. Rev. D **44**, 1415 (1991); **45**, 1512 (1992); C. P. Yuan, Phys. Lett. B **283**, 395 (1992).
[51] G. Ciapetti and A. Di Ciaccio, in *Proceedings of the ECFA Large Hadron Collider Workshop* [4], Vol. II, p. 155.
[52] U. Baur and E. L. Berger, Phys. Rev. D **47**, 4889 (1993).
[53] H. Aihara *et al.* (DPF diboson study group) (in preparation).
[54] CDF Collaboration, F. Abe *et al.*, Phys. Rev. Lett. **64**, 152 (1990).
[55] CDF Collaboration, F. Abe *et al.*, Phys. Rev. Lett. **65**, 224 (1990); Phys. Rev. D **43**, 2070 (1991).
[56] G. Landsberg, in *Proceedings of the Workshop on Physics at Current Accelerators and Supercolliders*, Argonne, Illinois, 1993, edited by J. L. Hewett, A. R. White, and D. Zeppenfeld (Argonne National Laboratory Report No. ANL-HEP-CP-93-92, Argonne, IL, 1993), p. 303.
[57] C. Bilchak, R. Brown, and J. Stroughair, Phys. Rev. D **29**, 375 (1984).
[58] M. Bilenky *et al.*, Nucl. Phys. **B409**, 22 (1993).
[59] M. Bilenky *et al.*, Nucl. Phys. **B419**, 240 (1994).